

Computationally efficient 3D finite element modeling of RC structures

George Markou^{*1} and Manolis Papadrakakis²

¹*Alhosn University, Department of Civil Engineering, P.O.Box 38772, Abu Dhabi, UAE*
²*Institute of Structural Analysis & Seismic Research, National Technical University of Athens, 9 Iroon Polytechniou Str., Zografou Campus, GR-15780 Athens, Greece*

(Received April 4, 2012, Revised April 29, 2013, Accepted May 2, 2013)

Abstract. A detailed finite element modeling is presented for the simulation of the nonlinear behavior of reinforced concrete structures which manages to predict the nonlinear behavior of four different experimental setups with computational efficiency, robustness and accuracy. The proposed modeling method uses 8-node hexahedral isoparametric elements for the discretization of concrete. Steel rebars may have any orientation inside the solid concrete elements allowing the simulation of longitudinal as well as transverse reinforcement. Concrete cracking is treated with the smeared crack approach, while steel reinforcement is modeled with the natural beam-column flexibility-based element that takes into consideration shear and bending stiffness. The performance of the proposed modeling is demonstrated by comparing the numerical predictions with existing experimental and numerical results in the literature as well as with those of a commercial code. The results show that the proposed refined simulation predicts accurately the nonlinear inelastic behavior of reinforced concrete structures achieving numerical robustness and computational efficiency.

Keywords: reinforced concrete; smeared crack; embedded reinforcement; natural beam-column element; flexibility element

1. Introduction

A number of numerical models have been proposed for the analysis of Reinforced Concrete (RC) structures but none of them has managed to provide the desired combination, at an acceptable level, of accuracy, robustness and computational efficiency in predicting the nonlinear inelastic behavior of different types of RC structures and structural members. 1D beam-column elements, based on either concentrated plasticity models (plastic hinges, see Clough *et al.* 1965, Takizawa 1976, Bertero 1985, Ciampi and Nicoletti 1986, Mergos and Kappos 2008) or distributed plasticity (fiber models, see Zeris and Mahin 1988, Mazars *et al.* 2006, Navarro *et al.* 2007, Papaioannou *et al.* 2005, Saritas and Filippou 2009), have difficulties in predicting the mechanical behavior of 3D RC framed structures due to their inability in capturing shear behavior and local phenomena that affect the global response of the structure. The use of 2D plane stress finite

*Corresponding author, Assistant Professor, E-mail: g.markou@alhosnu.ae

element models (see Kwan and Billington 2001, Kwak and Kim 2001, Mazars *et al.* 2004, Kwak and Kim 2006, Jendele and Červenka 2009) can avoid some simplified assumptions that are inherent in 1D beam-column models, like the influence of shear stresses, but their inability of capturing the out of plane response made them inadequate for 3D full-scale structural analysis. Three-dimensional simulation with solid finite elements, based on triaxial stress-strain relationships and embedded rebars (see Cervera *et al.* 1987, Kotsovos and Pavlovic 1995, Ozbolt and Li 2001, Girard and Bastien 2002, Hartl and Handel 2002, Mirzabozorg and Ghaemian 2005, Spiliopoulos and Lykidis 2006, Sato and Naganuma 2007, Červenka and Papanikolaou 2008, Papanikolaou and Kappos 2009), provides the highest quality of approximation but it is hindered with high computational cost and in several cases lack of robustness.

The computational complexity of such detailed models makes their use impractical for full-scale simulations. Furthermore, with the use of numerically unstable material models, such as the smeared crack approach in concrete, the sensitivity of these models to various user-defined parameters becomes more pronounced. These difficulties led a number of researchers (see Jendele and Červenka 2009, Cervera *et al.* 1987, Kotsovos and Pavlovic 1995, Ozbolt and Li 2001, Girard and Bastien 2002, Hartl and Handel 2002, Mirzabozorg and Ghaemian 2005) to use higher order elements (20-noded and 27-noded hexahedral elements) in connection with high integration rules. The use of this type of 3D elements and unstable material models has a direct consequence on the efficiency of the numerical simulations, requiring many Newton-Raphson (NR) iterations per load step and thus considerable computational effort even for small-scale finite element models. 8-noded hexahedral elements combined with rod rebar elements were used by Hartl and Handel 2002, while as presented by (Papanikolaou and Kappos 2009, the *ATENA* software code (Červenka *et al.* 2008) was used with 8-noded hexahedral isoparametric elements combined with 2-noded rod elements for the reinforcement). Furthermore, ABAQUS, ANSYS and LS-DYNA software were compared in Cotsovos *et al.* 2009. The numerical study on these three software, which also use 8-noded hexahedral isoparametric elements combined with 2-noded rod elements for the reinforcement, showed that the required hexahedral element size had to be very small (1-3cm hexahedral edge size) in order for the analysis to proceed with an acceptable accuracy and numerical robustness. This modeling resulted into very fine meshes making this type of modeling impractical for real-scale RC structures.

In this work an 8-noded hexahedral isoparametric element is used for the simulation of concrete, based on an improved concrete material model originally proposed by Kotsovos and Pavlovic 1995. The material model of concrete was developed on the basis of experimental tests of concrete under multiaxial stress states (Kotsovos 1979), where cracking was treated as a complete sudden loss of stress for monotonic loading conditions and the only material parameter required is the uniaxial compressive strength of concrete. The reinforcement is modeled with an embedded steel bar simulated with the Natural Beam-Column Flexibility-Based (*NBCFB*) element. The geometric treatment of the embedded reinforcement allows the rebar elements to have any orientation inside the concrete solid elements while the shear and bending stiffness of the rebars are taken into consideration. The formulation of the *NBCFB* element follows the nonlinear state determination presented by Spacone *et al.* 1996 and the natural mode method which was introduced by Argyris and co-workers (see Argyris *et al.* 1979, 1998).

The above features of the detailed 3D finite element discretization of RC structures are incorporated into the proposed numerical model and validation of the obtained numerical results is performed with comparisons with experimental data and numerical results of different types of RC structural members, which are found in the literature (see Bresel and Scordelis 1963, Lefas 1988,

Červenka 1970). In this work the *ATENA* commercial software code (Červenka *et al.* 2008) was also used as a comparative tool for testing the accuracy and computational efficiency of the proposed formulation.

2. Embedded reinforcement in hexahedral concrete elements

Previous simulations with the embedded rebar reinforcement used 2-noded or 3-noded rod elements. Hence, the reinforcement is simulated as uniaxial element, without taking into consideration shear and bending stiffness. Although it is generally believed that shear and bending resistance of reinforcement is not significant, there are cases where the shear and bending resistance are important in capturing the nonlinear response of RC structural members. The discretization of the reinforcement is performed in this study with *NBCFB* elements which in addition to the consideration of shear and bending it was found to increase the numerical stability of the nonlinear incremental-iterative procedure due to its advanced formulation features. However, the choice of using 3D beam elements instead of uniaxial rod elements introduces some implementation issues. When 2-noded or 3-noded rod elements are used, the compatibility conditions between the end-nodes 1 and 2 of the rod and the corresponding hexahedral nodes (n1–n8) is enforced through the translational degrees of freedom (Fig. 1a) of the hexahedral faces intersecting with the rebar element. When beam elements are used, the compatibility of rotation between the hexahedral nodal displacements and the rotation of the rebar nodes that are located on the corresponding hexahedral faces, must be also enforced. This is achieved by computing the hexahedral face rotation and imposing the compatibility with the corresponding rotational degree of freedom (dof) of the rebar node.

Assuming that the angle $\bar{\theta}$ between the longitudinal axis of the rebar and the normal \bar{n} on the master triangle of the hexahedral face (Fig. 2) remains fixed before and after deformation, the required rotation can be derived through kinematic constraints. The assignment of a master triangle at each rebar node is performed prior to the analysis by detecting the three nearest hexahedral nodes of the corresponding face containing the rebar node. These three nodes $n2$, $n3$, $n6$ in Fig. 2 represent the master triangle of the rebar node 2 which controls the rotation of the corresponding rebar node.

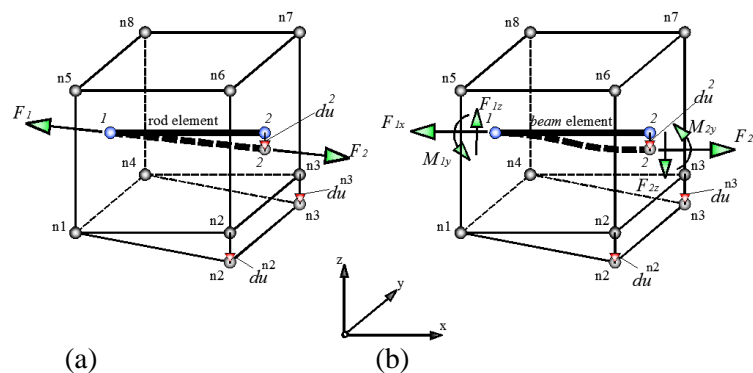


Fig. 1 Embedded rebar elements under imposed transverse deformation: (a) Rod element
(b) Beam element

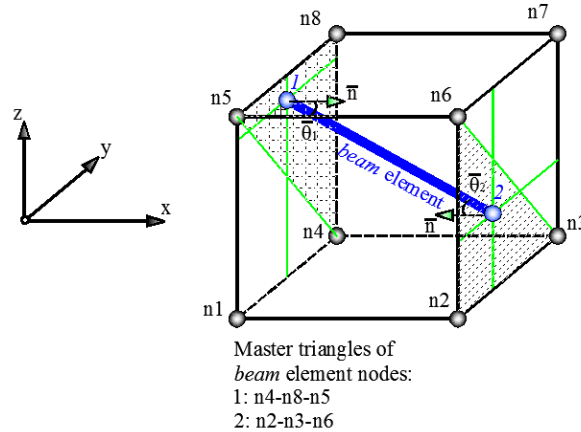


Fig. 2 Master triangles of beam element nodes 1 and 2

2.1 Kinematic constraints

Most researchers (Kotsovos and Pavlovic 1995, Ozbolt and Li 2001, Sato and Naganuma 2007, Barzegar and Maddipudi 1994, Elwi and Hruby 1989) use standard kinematic relations in order to connect the rod nodal displacements with the corresponding hexahedral displacements. A more recent approach was proposed by the Jendele and Červenka (2009) where the solution of a multi-point constraint conditions problem called Complex Boundary Conditions is performed. This procedure requires the solution of a system of non-symmetric constraint equations.

For the purpose of the present implementation, the kinematic relations that connect the beam nodal displacements with the nodal translations of the corresponding hexahedral face, are given from the following expressions

$$\mathbf{u}^B = \mathbf{T} \cdot \mathbf{U}^H, \quad \mathbf{F}^H = \mathbf{T}^T \cdot \mathbf{F}^B \tag{1}$$

(12×1) (12×24) (24×1) (24×1) (24×12) (12×1)

where \mathbf{u}^B and \mathbf{U}^H are the displacement vectors of the beam and hexahedral elements, respectively, while \mathbf{F}^B and \mathbf{F}^H are the corresponding internal force vectors. The transformation matrix \mathbf{T} is composed of 32 (3×3) submatrices which are computed from the natural coordinates of the hexahedral, the beam element and the master triangle nodes.

$$\mathbf{T}_{(12 \times 24)} = \begin{bmatrix} \mathbf{T}_1^1 & \mathbf{T}_2^1 & \mathbf{T}_3^1 & \mathbf{T}_4^1 & \mathbf{T}_5^1 & \mathbf{T}_6^1 & \mathbf{T}_7^1 & \mathbf{T}_8^1 \\ 0 & 0 & 0 & \mathbf{R}_4^1 & \mathbf{R}_5^1 & 0 & 0 & \mathbf{R}_8^1 \\ \mathbf{T}_1^2 & \mathbf{T}_2^2 & \mathbf{T}_3^2 & \mathbf{T}_4^2 & \mathbf{T}_5^2 & \mathbf{T}_6^2 & \mathbf{T}_7^2 & \mathbf{T}_8^2 \\ 0 & \mathbf{R}_2^2 & \mathbf{R}_3^2 & 0 & 0 & \mathbf{R}_6^2 & 0 & 0 \end{bmatrix}, \tag{2}$$

The submatrices located in rows 1 and 3 of \mathbf{T} correspond to the translational rebar displacements \mathbf{T}_i^j and those in rows 2 and 4 correspond to the rotational rebar displacements \mathbf{R}_m^j . Eq. (2) refers to the case illustrated in Fig. 2 where the nodes 1 and 2 of the rebar correspond to $(n4 - n8 - n5)$ and $(n2 - n3 - n6)$ master triangles, respectively.

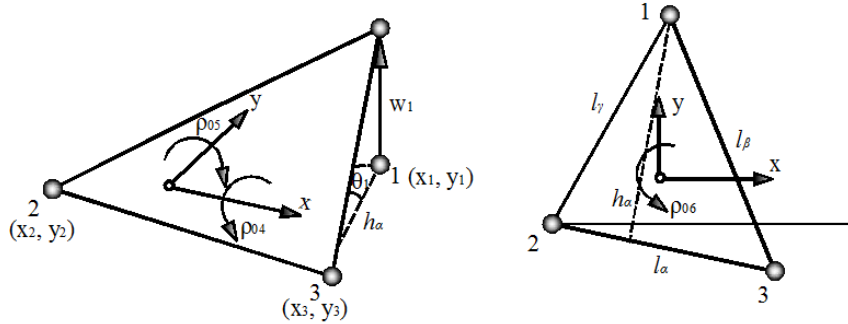


Fig. 3 Rotation θ_l

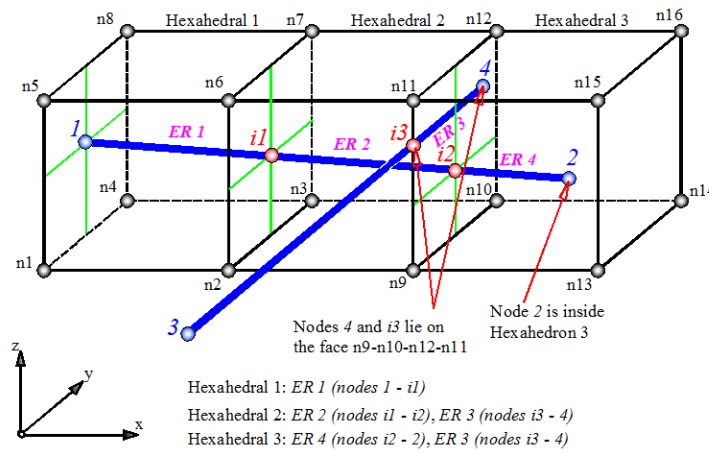


Fig. 4 Embedded reinforcement inside hexahedral elements

Each transformation matrix \mathbf{T} (Eq. (2)) consists of 22 non-zero submatrices with dimension 3×3 . From Eq. (2) it can be seen that the translational dof of each beam element node are transformed through the use of \mathbf{T}_i^j matrices

$$\mathbf{T}_i^j = \begin{bmatrix} N_i^j & 0 & 0 \\ 0 & N_i^j & 0 \\ 0 & 0 & N_i^j \end{bmatrix}, \quad (3)$$

where N_i^j ($i = 1, 8$) correspond to the 8 hexahedral shape functions and $j = 1, 2$ denote the embedded rebar nodes. After the computation of the value of each shape function N_i^j at the natural coordinates of each beam node the corresponding matrices are assembled. As it can be seen from Eq. (3), submatrix \mathbf{T}_i^j contains the shape function value N_i computed at the rebar node j .

In order to handle the rotational dof of the embedded rebar beam element, the definition of a

master triangle is necessary in order to compute the rotation along the three global axes. This master triangle is formed with the three nearest nodes to the rebar beam element node of the corresponding hexahedral face (Fig. 2). The computation of each master triangle rigid body rotations is performed with the natural mode concept of Argyris *et al.* 1997 (Appendix D).

2.2 Generating reinforcement in FE modeling

The most notable method for the generation of rebar reinforcement elements in FE modeling of concrete structures is proposed by Barzegar and Maddipudi 1994, which is an extension of the work of Elwi and Hrudey 1989. This approach has the advantage of allowing arbitrary positions for the rebars inside the concrete elements and a free geometry for the hexahedral elements. For this purpose, a nonlinear search procedure based on the NR method is required in order to calculate the natural coordinates of each steel bar node. Despite the fact that the convergence rate of the nonlinear search is rather high, the computational demand for relatively large-scale structures with thousands of steel rebars becomes excessive. In order to reduce the computational cost for generating rebar reinforcement, a geometrical constraint during the rebar search process is proposed in this work making its numerical implementation less computationally demanding.

The proposed method considers arbitrary positioning of the rebars inside the concrete elements, as shown in Fig. 4, while avoiding a nonlinear search procedure the calculation of the natural coordinates of the embedded reinforcement nodes for each hexahedral element.

The developed finite element code *ReConAn* (Markou 2010) uses the initial rebar node coordinates that were created with Femap software (Siemens 2009) and generates the geometry of the embedded rebars. The generation of the embedded rebar elements is performed for each initial rebar separately by performing an independent search in order to detect all its intersections with the surrounding solid elements. The outcome of this arithmetic procedure is the location of the embedded rebar elements in the corresponding hexahedral elements.

Generation of embedded virtual nodes

The virtual nodes correspond to the intersections of the rebars with hexahedral faces ($i1, i2, i3$ in Fig. 4). This procedure becomes cumbersome when the FE model consists of a large number of hexahedral and rebar elements. It is evident that if we attempt to compute these possible intersection points without implementing any constraint on the search space, the computational cost of the search algorithm will be significant. The problem arises from the fact that it is required to locate all possible intersections that may exist between the hexahedral faces and the initial rebar geometry (Figs. 5-6).

To avoid unnecessary calculations, a geometric constraint was introduced in order to restrict the search in the vicinity of the corresponding steel reinforcement. The geometric constraint is implemented with the definition of an active sphere with radius R_c

$$R_c = c \cdot L, \quad (4)$$

where

$$L = \sqrt{s_x^2 + s_y^2 + s_z^2} \quad (5)$$

and

$$s_x = \frac{\left(\sum_{n=1}^8 (s_x^{cen} - s_x^n) \right)}{8}, \quad s_y = \frac{\left(\sum_{n=1}^8 (s_y^{cen} - s_y^n) \right)}{8}, \quad s_z = \frac{\left(\sum_{n=1}^8 (s_z^{cen} - s_z^n) \right)}{8} \quad (6)$$

with s^n and s^{cen} being the coordinates of the node n and the centroid of the hexahedral under consideration, respectively, while parameter c defines the active volume around each hexahedral where the constraint is implemented. Then the search is performed only when the following relation is satisfied,

$$d_{n1}^i \text{ or } d_{n2}^i < R_c \quad (7)$$

where $d_{n1}^i = |s_i^{cen} - s_{rebar}^{n1}|$, $d_{n2}^i = |s_i^{cen} - s_{rebar}^{n2}|$ are the distances of the rebar end nodes 1 and 2 from the hexahedral centroid i under consideration as it is illustrated in Fig. 6.

After an extensive parametric investigation the recommended value for the incremental parameter c was found to be equal to 5, which was used in our numerical implementations. Larger values for c would lead to unnecessary computations for the location of possible rebar-hexahedral face intersections, while smaller values would make the generation of the initial rebar mesh more complicated and time consuming. This value is related to the maximum penetrated hexahedral elements by a rebar member in order to assure that at least one rebar node will be located inside the hexahedral active sphere, as illustrated in Fig. 6. The proposed constraint technique reduces the computational effort since it allows less neighboring hexahedral elements to be checked during the rebar allocation stage.

After the satisfaction of the constraint Eq. (7), the generation of the reinforcement rebar elements proceeds according to the following three cases.

Case 1

In this case, a check is performed to detect whether one or both rebar nodes (1, 2) are located on a hexahedral face (Fig. 7a). Before moving to the computation of the natural coordinates of the virtual node a check if the hexahedral shape is orthogonal or irregular is performed. If the shape is orthogonal then in order to locate the position of the corresponding rebar node, the distances d_x , d_y and d_z between the hexahedral centroid and the rebar node need to be computed. These distances are given by

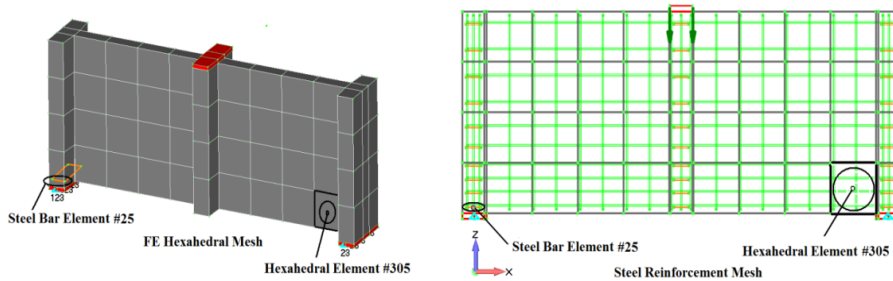


Fig. 5 Concrete FE mesh and steel reinforcements

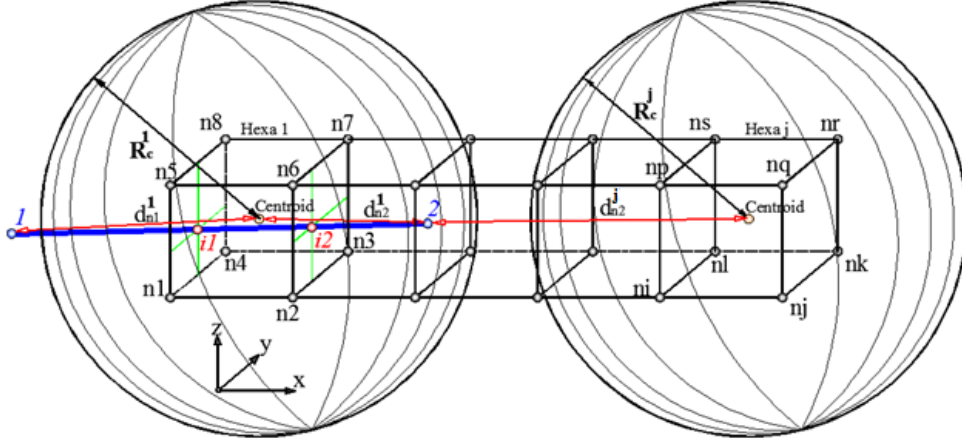


Fig. 6 Geometric constraint for the search of embedded rebar nodes: (a) Geometric constraint is satisfied: $R_c^1 > d_{n2}^1$; (b) $R_c^j < d_{n2}^j < d_{n1}^j$ Geometric constraint is not satisfied: $R_c^i < d_{n2}^i < d_{n1}^i$

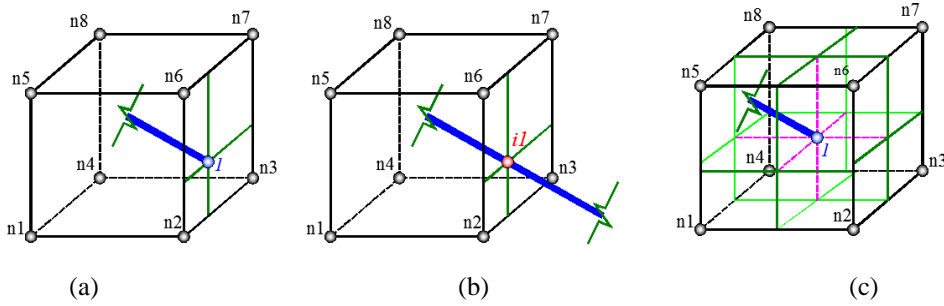


Fig. 7 Geometric configuration of the three cases. (a) Case 1: Rebar node on a hexahedral face; (b) Case 2: Rebar-hexahedral face intersection; (c) Rebar node inside the hexahedral volume

$$d_x = s_x^{n1} - s_x^{cen}, \quad d_y = s_y^{n1} - s_y^{cen}, \quad d_z = s_z^{n1} - s_z^{cen} \quad (8)$$

Finally the natural coordinates of any given point P of the rebar inside a hexahedral, are given from the following expressions

$$\xi_P = \frac{s_x^P - s_x^{cen}}{d_x}, \quad \eta_P = \frac{s_y^P - s_y^{cen}}{d_y}, \quad \zeta_P = \frac{s_z^P - s_z^{cen}}{d_z} \quad (9)$$

If the rebar is located on a hexahedral face, then the proposed algorithm searches for intersections with the hexahedral face edges and creates the corresponding virtual nodes of the rebar finite element (nodes 4, $i3$ in Fig. 4). For this subcase, the stiffness matrix of the embedded rebar finite element (element ER 3 in Fig. 4) is distributed between the two neighboring hexahedral elements (Hexahedral 2 and 3 in Fig. 4). Moreover, in order to avoid the warping problem during the computations of the rebar nodal rotations, this type of rebar are treated as uniaxial elements.

For the case where the hexahedral element shape is irregular, then the standard Barzegar and Maddipudi 1994 method (Appendix B) is performed in order to allocate the natural coordinates of the corresponding virtual node.

Case 2

In the second case, the rebar intersects with one or two hexahedral faces as illustrated in Fig. 7b. It is important to note here that all hexahedral faces are described by algebraic plane equations which are used in order to find a potential line-plane intersection, as described in Appendix A. Subsequently, if an intersection exists it has to be verified if it is located inside the hexahedral face bounded by the four hexahedral face nodes.

The following constraint guaranties that the line-plane intersection is located inside the face of the hexahedral under consideration

$$|\xi_p, \eta_p, \zeta_p| \leq 1 \tag{10}$$

where ξ_p, η_p, ζ_p are the natural coordinates of the intersection point. If this constraint is not satisfied, the intersection point is not retained (*i3* in Fig. 8) and the algorithm proceeds with the computation of the next intersection point.

Case 3

When cases 1 and 2 are not applicable, then a check is performed whether the constraint

$$|\xi_p, \eta_p, \zeta_p| < 1 \tag{11}$$

is satisfied, where ξ_p, η_p, ζ_p are the natural coordinates of the rebar node obtained either from Eq. (9) or from the Barzegar and Maddipudi procedure, depending on the element shape. If the above

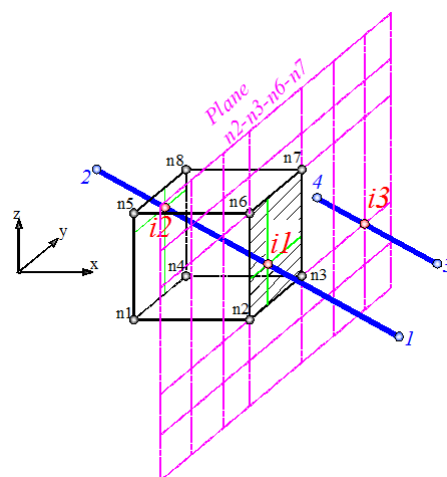


Fig. 8 Initial rebar element intersections with hexahedral faces. Nodes *i1* and *i2* are retained, node *i3* is not acceptable

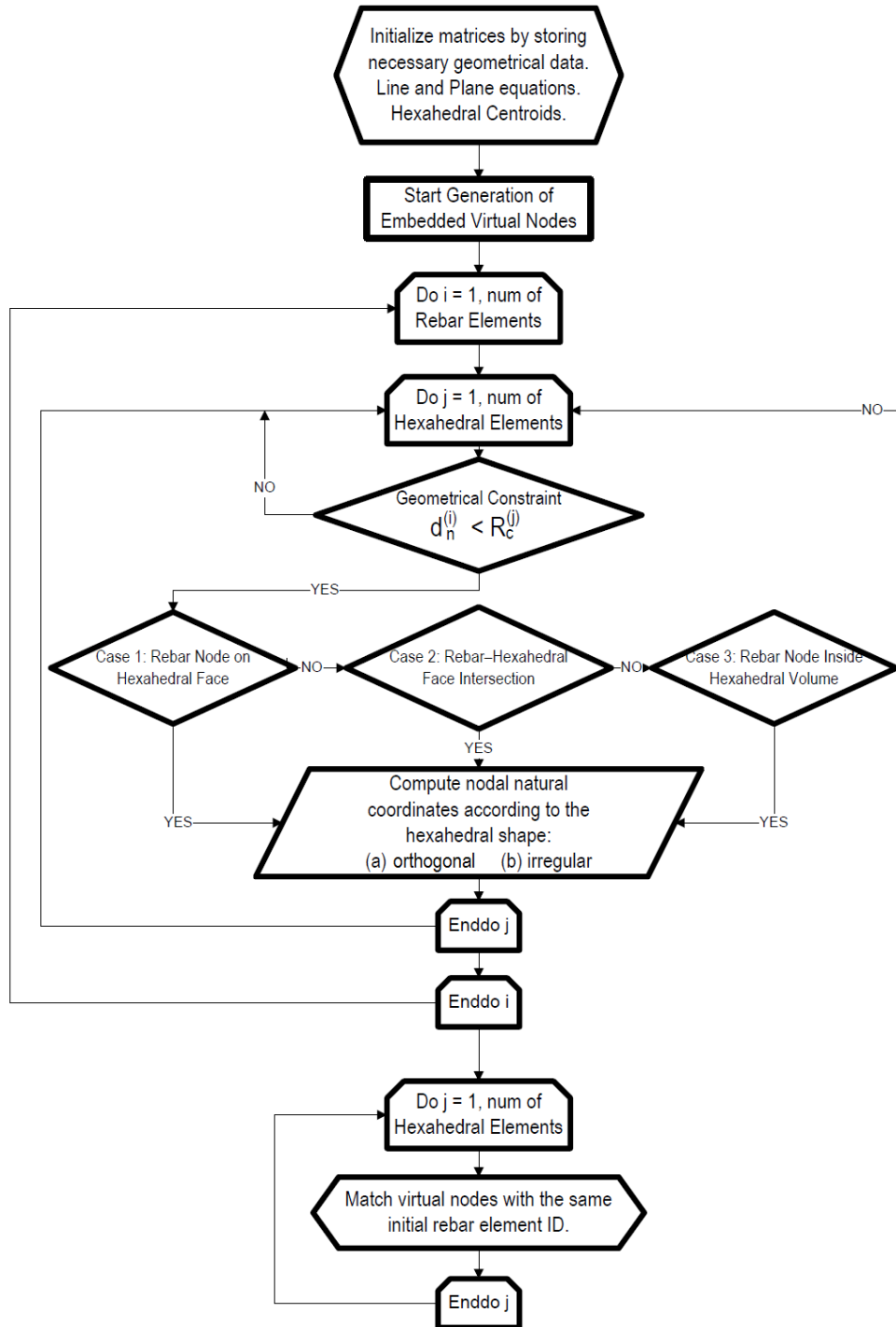


Fig. 9 Flow chart of the proposed embedded rebar element mesh generation method (Markou and Papadrakakis 2012)

inequality is satisfied, it means that the rebar node is located inside the volume of the hexahedral (Fig. 7c) and it is stored for further consideration, otherwise the node is located outside the hexahedral volume and no further action is taken. After the computation of the virtual nodes of the initial reinforcement grid, the mesh generation of the embedded rebar finite elements is performed.

Following the described generation algorithm, all necessary data of each hexahedral element is determined regarding the corresponding virtual rebar nodes that were located inside the volume or on its faces. At this point, the main features of the embedded rebar element are calculated and stored: The type of element (*Beam* or *Rod*), nodal coordinates, the type of nodes (if a node is virtual or a physical node of the initial mesh) and the material properties. Fig. 9 illustrates the flow chart of the proposed embedded rebar element mesh generation algorithm. It has to be mentioned that, in order for the nodal natural coordinate's computations to be applicable, hexahedral elements must be orthogonal parallelepipeds. If the hexahedral shape is irregular then the Barzegar and Maddipudi method, as described in the Appendix B, is used instead of Eq. (9).

2.3 Numerical implementation

In this section, a numerical verification of the efficiency of the proposed embedded reinforcement generation method will be presented. For this reason, two different FE models have been tested: A RC shear wall and a 3D RC frame. Different reinforcement properties and geometries are considered with the purpose of demonstrating the capability of the proposed method to allocate and generate embedded reinforcement elements with computational efficiency when dealing with large-scale models. All numerical tests were performed on a laptop with a 1.9GHz processor and a 2GB DDR2 Ram.

2.3.1 RC shear wall

The RC shear wall consists of 1,680 hexahedral elements ($0.10 \text{ m} \times 0.125 \text{ m} \times 0.0767 \text{ m}$) and 1,320 initial rebars (vertical reinforcement $\emptyset 12/10$ and horizontal reinforcement $\emptyset 8/15$). As can be seen in Fig. 10, the RC shear wall has a total length of 2.80 m, a height equal to 2.30 m and a 0.25 m thickness. The embedded rebar mesh generation procedure terminates the generation with the allocation of 3,080 rebar finite elements in 1.1 seconds.

In order to test the proposed generation framework for larger discretizations we considered a tenfold increase of the previous model. The new FE model consists of 17,080 hexahedral elements and 13,192 initial rebar elements (Fig. 11). After the completion of the embedded rebar element mesh generation process, the total number of generated embedded rebar finite elements becomes 34,327 and the corresponding required computational time is 85 sec. The proposed algorithm managed to scan and generate all the embedded reinforcement elements within an affordable computational time. This is mainly attributed to the implementation of the geometric constraint of Eq. (7). The corresponding computational time for the embedded rebar element mesh generation process, when the geometrical constraint is not used, was 7 min. This shows the importance of the proposed constraint during the mesh generation process particularly for large-scale models. Since the required CPU time for the embedded mesh generation procedure cannot be explicitly measured when ATENA software is used, the comparison cannot be made for this case. Nevertheless, the required initiation CPU time, for these two numerical tests, were 3 and 25 min, respectively. The corresponding CPU times of ReConAn are 2 and 160 sec (including the embedded rebar mesh generation procedure). These differences are to a certain extent attributed to I/O procedures that ATENA performs during the initialization of the models.

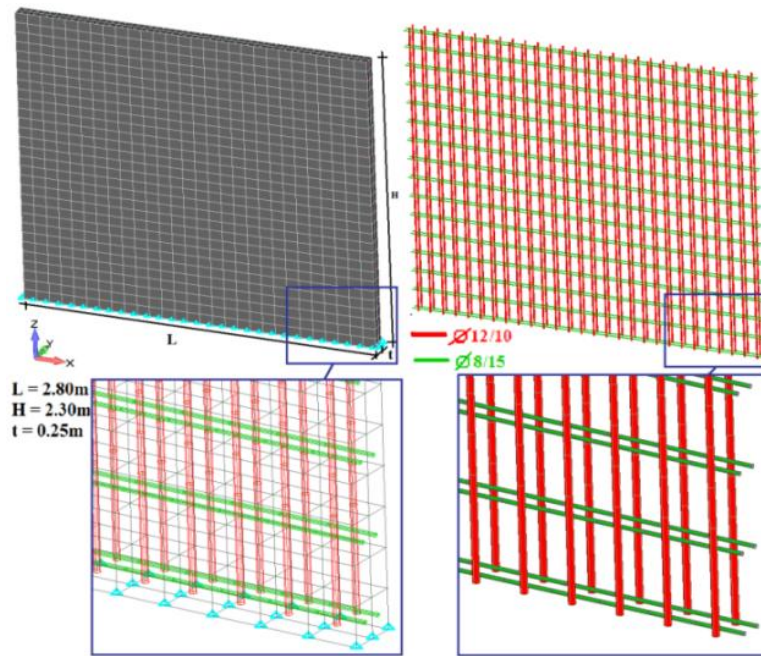


Fig. 10 RC shear wall with 1,680 hexahedral elements and 1,320 initial rebar elements

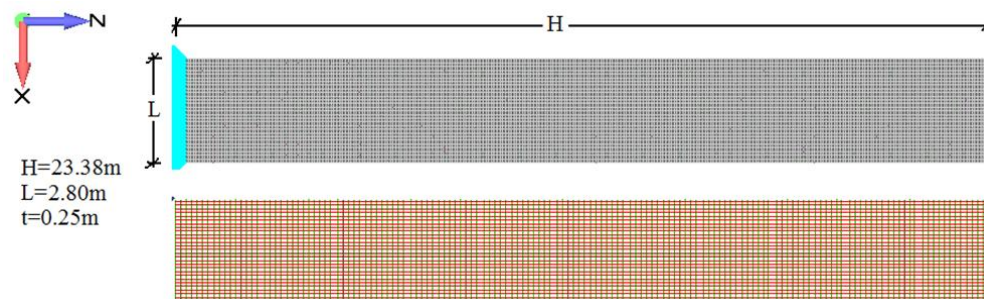


Fig. 11 RC shear wall with 17,080 hexahedral elements and 13,192 initial steel bar elements

2.3.2 RC frame

This model was created with the purpose of illustrating the ability of the proposed algorithm to generate embedded reinforcement for more complicated reinforcement layouts. The rebar layout for each structural member is depicted in Fig. 12. The RC frame has a 5 m span and consists of a shear wall, a beam, a column and two foundation footings in order to make the geometry more complex.

Fig. 13 illustrates the initial discretization with hexahedral and rebar elements. The initial FE model The total number of embedded rebar elements created after the execution of the rebar element mesh generation process was 4,434 and the corresponding required time was 5 seconds. It can be seen that the mesh generation is completed in a minimal computational time despite the fact that the mesh of the hexahedral elements was very dense, especially in the foundation footings.

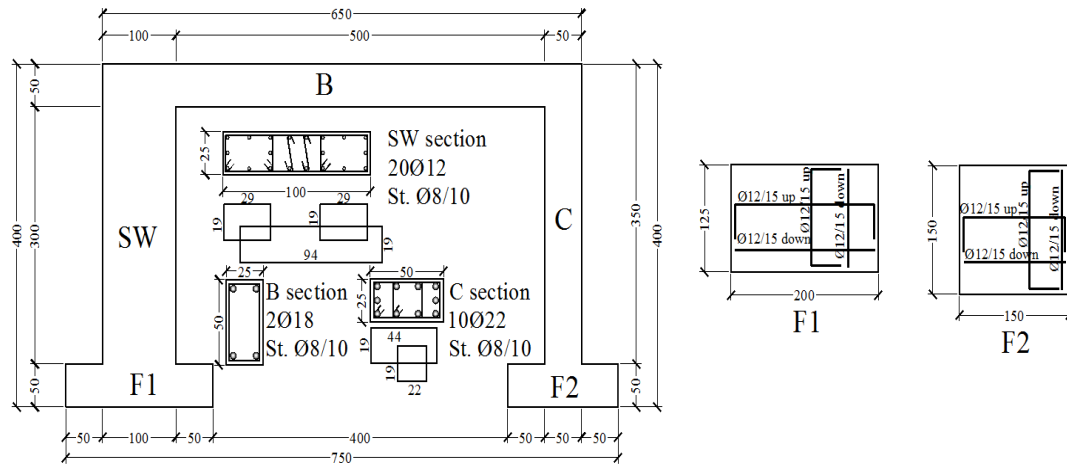


Fig. 12 RC frame. Geometry and reinforcement details

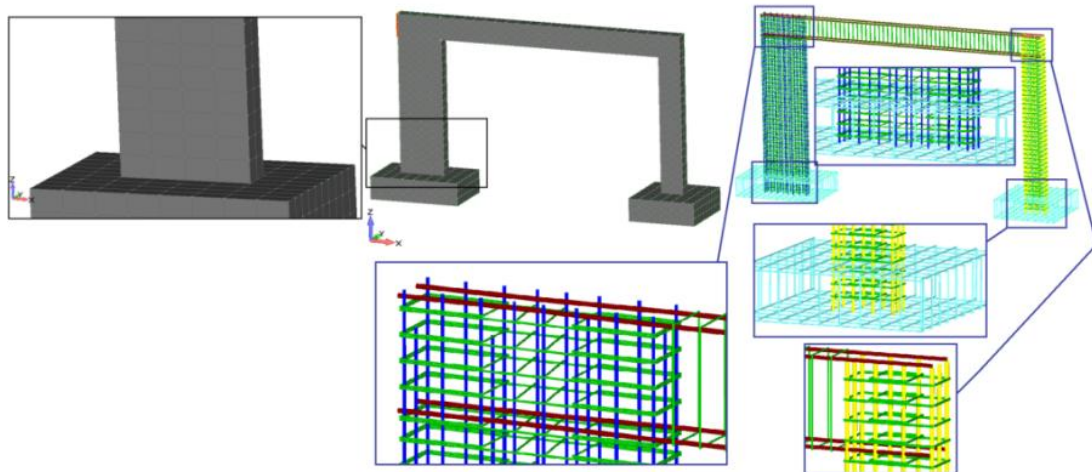


Fig. 13 RC frame. Initial FE mesh (Hexahedral elements – Reinforcement mesh)

2.4 The NBCFB element

The Natural Beam-Column Flexibility-Based (*NBCFB*) element (Papaioannou *et al.* 2005, Papachristidis *et al.* 2009 and 2010) is a 2-noded three-dimensional beam finite element with 12 degrees of freedom (6 per node). The computation of its flexibility-based stiffness matrix is done with the use of Gauss-Lobato integration points. The flexibility-based formulation relies on force interpolation functions that strictly satisfy the equilibrium of bending moments and axial force along the element and requires an iterative algorithm in order to calculate the internal forces during the element state determination, as described by Spacone *et al.* 1996.

Assuming that xyz axes represent the global coordinate system, the nodal displacements are grouped in the vector (see Fig. 14)

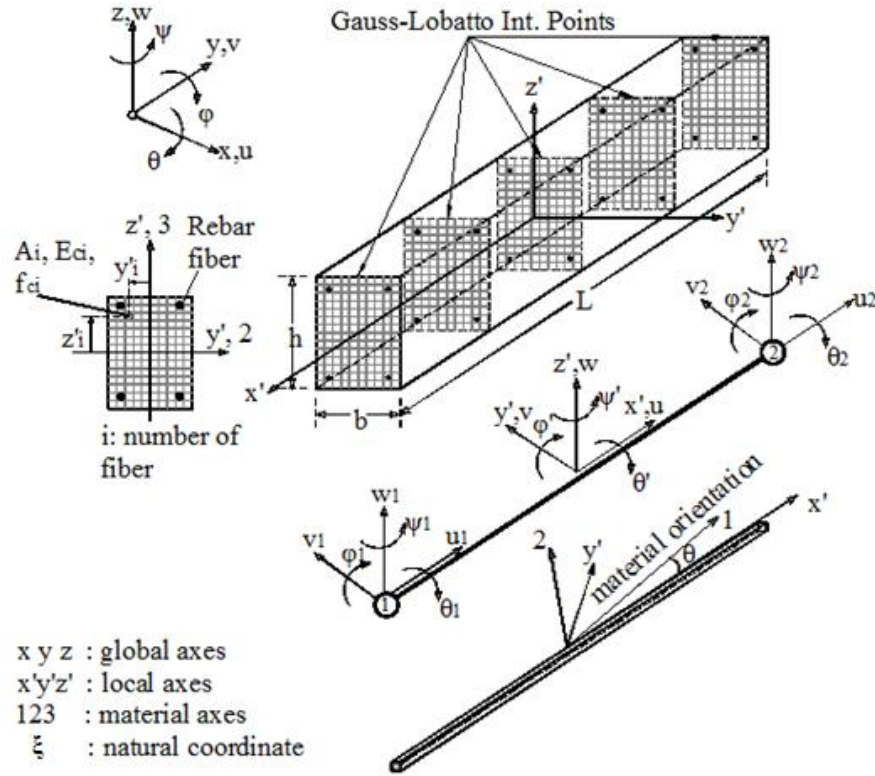


Fig. 14 RC fiber beam elements in space

$$\boldsymbol{\rho} = [u_1 \quad v_1 \quad w_1 \quad \theta_1 \quad \varphi_1 \quad \psi_1 \quad u_2 \quad v_2 \quad w_2 \quad \theta_2 \quad \varphi_2 \quad \psi_2] \quad (12)$$

where \$u, v\$ and \$w\$ represent the translational dof and \$\theta, \varphi\$ and \$\psi\$ denote the rotational dof. These dof can refer either to a global or a local Cartesian coordinate system which are related through transformation matrices that contain directional cosines.

A local Cartesian coordinate system \$x'y'z'\$ is assigned to the element and it is placed at its centroid to which local Cartesian dof are referred to

$$\bar{\boldsymbol{\rho}} = [\bar{u}_1 \quad \bar{v}_1 \quad \bar{w}_1 \quad \bar{\theta}_1 \quad \bar{\varphi}_1 \quad \bar{\psi}_1 \quad \bar{u}_2 \quad \bar{v}_2 \quad \bar{w}_2 \quad \bar{\theta}_2 \quad \bar{\varphi}_2 \quad \bar{\psi}_2] \quad (13)$$

A natural coordinate \$\xi\$ spanning the beam's axis is adopted, which coincides with the local Cartesian axis \$x'\$. The local Cartesian dof are transformed into natural invariant rigid body and straining modes \$\rho_0, \rho_N\$, respectively, so that a unique and reversible relation exists between the natural modes and the local and global dof in the sense

$$\underset{(12 \times 1)}{\boldsymbol{\rho}} \Leftrightarrow \underset{(12 \times 1)}{\bar{\boldsymbol{\rho}}} \Leftrightarrow \left[\underset{(1 \times 6)}{\boldsymbol{\rho}_0^T}, \underset{(1 \times 6)}{\boldsymbol{\rho}_N^T} \right]^T \quad (14)$$

When fibers are considered, an additional coordinate system is defined for every fiber (i), namely the 123 coordinate system, with axis 1 along the longitudinal reinforcement direction and axes 2 and 3 perpendicular to it. Note that material axis 3 is parallel to the local Cartesian axis z' . Then, for every fiber k , axis 1 forms an angle θ_k , with the local axis x' (see Fig. 14). Therefore, the *NBCFB* element comprises 12 Cartesian dof but the actual number of straining modes is 6.

The two main differences of the flexibility-based element compared to the classical stiffness element are that the element stiffness matrix is calculated by inverting the flexibility matrix and that the element state determination begins from the elements internal force equilibrium. These two features enhance the numerical robustness and increase the accuracy of the incremental nonlinear solution procedure with respect to the size of the load steps. This property derives from the fact that the internal nonlinear state determination procedure computes the exact equilibrium solution, between the resisting forces and the nodal displacements of each element, inducing numerical stability in the incremental nonlinear solution procedure of the structure.

2.4.1 Stiffness matrix of embedded *NBCFB* elements

In order to extract the force distribution $\mathbf{D}(\xi)$ along the element from the generalized force vector \mathbf{Q} the interpolation functions $\mathbf{b}(\xi)$ are defined as follows

$$\mathbf{b}(\xi) = \begin{Bmatrix} 1 & . & . & . & . & . \\ . & -1 & \xi & . & . & . \\ . & . & . & -1 & \xi & . \end{Bmatrix} \quad (15)$$

where ξ is the natural coordinate of the corresponding control-section of the Gauss-Lobato integration rule implemented for this element.

When one of the sections enters into the nonlinear strain-stress field for the first time an update of the sections stiffness matrix is necessary. By storing the areas A_{ifiber} of all fibers in vector \mathbf{A} and the corresponding Young modulus E_{ifiber} in \mathbf{E} , the section tangent stiffness matrix is derived from

$$\mathbf{k}^j(\xi) = \mathbf{l}^T(\xi) (\mathbf{E}_{ifiber}^j \cdot \mathbf{A}_{ifiber}) \mathbf{l}(\xi) \quad (16)$$

where $\mathbf{l}(\xi)$ is a compatibility matrix containing the local coordinates of each fiber. Eq. (16) results in

$$\mathbf{k}^j(\xi) = \begin{bmatrix} \sum_{ifiber=1}^{nfibers} E_{ifiber}^j \cdot A_{ifiber} & - \sum_{ifiber=1}^{nfibers} E_{ifiber}^j \cdot A_{ifiber} \cdot z_{ifiber} & \sum_{ifiber=1}^{nfibers} E_{ifiber}^j \cdot A_{ifiber} \cdot y_{ifiber} \\ - \sum_{ifiber=1}^{nfibers} E_{ifiber}^j \cdot A_{ifiber} \cdot z_{ifiber} & \sum_{ifiber=1}^{nfibers} E_{ifiber}^j \cdot A_{ifiber} \cdot z_{ifiber}^2 & - \sum_{ifiber=1}^{nfibers} E_{ifiber}^j \cdot A_{ifiber} \cdot z_{ifiber} \cdot y_{ifiber} \\ \sum_{ifiber=1}^{nfibers} E_{ifiber}^j \cdot A_{ifiber} \cdot y_{ifiber} & - \sum_{ifiber=1}^{nfibers} E_{ifiber}^j \cdot A_{ifiber} \cdot z_{ifiber} \cdot y_{ifiber} & \sum_{ifiber=1}^{nfibers} E_{ifiber}^j \cdot A_{ifiber} \cdot y_{ifiber}^2 \end{bmatrix} \quad (17)$$

where $\mathbf{k}^j(\xi)$ is the sectional stiffness matrix (Spacone *et al.* 1996) located at the natural coordinate ξ . The updated natural stiffness matrix of the *NBCFB* element is obtained via the

flexibility matrix F , which is computed as the sum tangent or elastic flexibility matrices $f^j(\xi)$ according to Eq. (18).

$$\mathbf{F}_{(6 \times 6)} = \sum_{iSection=1}^{nSections} \mathbf{b}^T(\xi)_{(6 \times 3)} \cdot \mathbf{f}^{iSection}(\xi)_{(3 \times 3)} \cdot \mathbf{b}(\xi)_{(3 \times 6)} \cdot w^{iSection} \quad (18)$$

where the w parameter represents the section's integration weight factor and $f^j(\xi) = [\mathbf{k}^j(\xi)]^{-1}$. Finally, by inverting the natural flexibility matrix F the tangential natural stiffness matrix of the beam is obtained

$$\left[\mathbf{K}_{Natural}^{beam} \right]_{(6 \times 6)} = \left[\mathbf{F}_{beam} \right]_{(6 \times 6)}^{-1} \quad (19)$$

The final step for computing the global elemental stiffness matrix is to perform the standard transformation

$$\mathbf{K}_{Cartesian}^{beam} = \left[\begin{array}{c} \mathbf{T}_{04}^T \left[\begin{array}{ccc} \bar{\mathbf{a}}_N^T \left[\mathbf{K}_{Natural}^{beam} \right] \bar{\mathbf{a}}_N \end{array} \right] \mathbf{T}_{04} \\ \underbrace{\hspace{10em}}_{\text{local Cartesian stiffness matrix } \bar{\mathbf{k}}} \\ \underbrace{\hspace{10em}}_{\text{global Cartesian stiffness matrix } \mathbf{k}} \end{array} \right] \quad (20)$$

where $\bar{\mathbf{a}}_N$ is the connection matrix which contains only geometrical parameters (Argyris *et al.* 1998). \mathbf{T}_{04} is a matrix that contains submatrices of direction cosines (Argyris *et al.* 1997).

2.4.2 Nonlinear internal state determination process

In order to describe the nonlinear internal state determination process, the definition of the equilibrium equation must be given. Eq. (21) expresses the linearized relation between the applied unbalanced forces $\mathbf{P}^i - \mathbf{Q}^{i-1}$ and the corresponding incremental displacements $\Delta \mathbf{q}^i$ at the element level (Spacone *et al.* 1996)

$$\left[\mathbf{F}^{i-1} \right]^{-1} \cdot \Delta \mathbf{q}^i = \mathbf{P}^i - \mathbf{Q}^{i-1} \quad (21)$$

Since the section internal resisting forces $\mathbf{D}_R^j(\xi)$ cannot be obtained directly from the section force-deformation relation, they are determined by summation of the axial force and biaxial bending contribution of all the fibers of the section as shown below

$$\mathbf{D}_R^j(\xi) = \mathbf{l}^T(\xi) \cdot \mathbf{E}^j \cdot \mathbf{A} \quad (22)$$

and after carrying the multiplications

$$\mathbf{D}_R^j(\xi) = \left\{ \begin{array}{l} \sum_{ifiber=1}^{nfibers} \sigma_{ifiber}^j \cdot A_{ifiber} \\ - \sum_{ifiber=1}^{nfibers} \sigma_{ifiber}^j \cdot A_{ifiber} \cdot z_{ifiber} \\ \sum_{ifiber=1}^{nfibers} \sigma_{ifiber}^j \cdot A_{ifiber} \cdot y_{ifiber} \end{array} \right\} \quad (23)$$

The end-node force vector \mathbf{Q} is computed from the section internal resisting forces $\mathbf{D}_R^j(\xi)$ as follows

$$\mathbf{Q} = \sum_{iSection=1}^{nSections} \mathbf{b}^T(\xi) \cdot \mathbf{D}_R^{iSection}(\xi) \cdot w^{iSection} \quad (24)$$

$(6 \times 1) \quad (6 \times 3) \quad (3 \times 1)$

where w is the parameter that represents the sections Gauss-Lobato integration weight factor and $\mathbf{b}(\xi)$ contains the interpolation functions (Eq. 15). Finally, the elemental internal forces with respect to the global system are computed from

$$\mathbf{P}_{internal} = \mathbf{T}_{04}^T \cdot \mathbf{a}_n^T \cdot \mathbf{Q} \quad (25)$$

$(12 \times 1) \quad (12 \times 12) \quad (12 \times 6) \quad (6 \times 1)$

After the computation of the elemental internal forces the internal state determination procedure is performed as it is described by Spacone *et al.* 1996 (Appendix C). The state determination procedure is integrated with the natural mode method (Argyris *et al.* 1979, 1998).

2.4.3 Idealization of the rebar elements

As can be seen in Fig. 15, the section of any rebar may be transformed into an equivalent square section which is subdivided into a number of fibers in x and y directions. The idealization of the rebar's section into square is performed in order to simplify the discretization procedure. Given the diameter of the rebar, the

dimensions of the square cross section are given by

$$b = h = \sqrt{\frac{\pi d^2}{4}} \quad (26)$$

The material law adopted in this work for the inelastic modeling of the steel rebars was the one proposed by Menegotto and Pinto 1973.

Numerical tests performed for both cross sections produced identical results since the stiffness coefficients that are mainly affected through the sectional simplification correspond to the bending coefficient which is by nature much smaller than the corresponding axial and shear coefficients of the rebar.

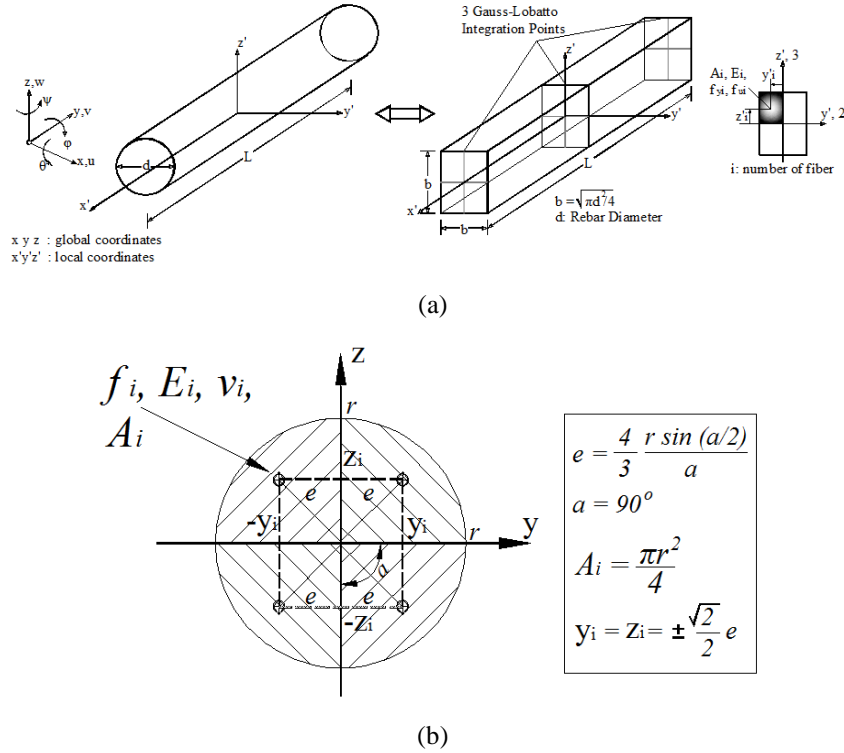


Fig. 15 Discretization of (a) a square and (b) a circular section with fibers

2.4.4 Transformation of the stiffness matrix of the embedded NBCFB elements

The contribution of the rebar stiffness to the stiffness matrix of the parent hexahedral element is given by

$$\widehat{\mathbf{K}}_{Hexa} = \mathbf{K}_{Hexa} + \sum_{i=1}^{nr} (\mathbf{T}_i)^T \cdot \mathbf{K}_i^{rebar} \cdot \mathbf{T}_i \tag{27}$$

(24×24) (24×24) (24×12) (12×12) (12×24)

where \mathbf{T}_i is the transformation matrix given in Eq. (2) for imposing the compatibility condition between the rebar and the corresponding hexahedral's nodal displacements. \mathbf{K}_{Hexa} is the stiffness matrix of the hexahedral concrete element and nr is the number of rebars embedded in the element.

3. Concrete 3D material model

Several material models have been proposed or studied for the modeling of concrete (Fardis *et al.* 1983, Kolleger and Mehlhorn 1987, Simo and Ju 1987, Lubliner *et al.* 1989, Armero and Oller 2000, Balan *et al.* 2001, Lee and Fenves 2001, Nechnech *et al.* 2002, Borja *et al.* 2003, Park and Kim 2005, Jason *et al.* 2006, Desmorat *et al.* 2007, Oliver *et al.* 2008). A comprehensive review on

the progress made in the past years on concrete material models can be found in Lykidis 2007. The 3D material model for concrete implemented in this work was based on the Kotsovos and Pavlovic (1995) model after a modification of its numerical implementation in order to improve its numerical robustness. In the following, the Kotsovos and Pavlovic model will be briefly presented as well as the proposed modifications.

3.1 Concrete constitutive model

The experimental data on concrete behavior used for the development of constitutive laws are obtained from tests on specimens such as cylinders, prisms and cubes. Such specimens are subjected to various load combinations, usually applied through rigid steel plates (compressive test or triaxial test). The obtained results are expressed in the form of stress-strain curves, which consist of a strain hardening branch followed by a strain softening one. After extensive experimental work (Kotsovos 1983, van Mier 1986, van Mier *et al.* 1997), it was found that only strain hardening may describe material behavior under a definable state of stress. It was concluded that the strain softening branch basically reflects the interaction between specimens and loading platens (Fig. 16), with the development of uncontrolled frictional stresses on the faces between the specimen and the loading device.

The generalized stress-strain relationships, corresponding to the ascending branch of concrete materials, can be expressed by decomposing each state of stress into a hydrostatic (σ_0) and a deviatoric component (τ_0) which represent the normal and shear octahedral stresses. The hydrostatic and deviatoric stresses derive from the corresponding hydrostatic and deviatoric strains (ε_0, γ_0) from the following relationships

$$\varepsilon_0 = \varepsilon_{0h} + \varepsilon_{0d} = \frac{\sigma_0 + \sigma_{id}}{3K_S}, \quad \gamma_0 = \frac{\tau_0}{2G_S} \quad (28)$$

where $\sigma_{id}(\sigma_0, \tau_0, f_c)$ is an equivalent internal hydrostatic stress that accounts for the coupling between τ_0 and ε_{0d} , $K_S(\sigma_0, \tau_0)$ and $G_S(\sigma_0, \tau_0)$ are secant bulk and shear moduli, respectively, obtained by ignoring the coupling stress σ_{id} . The expressions for σ_{id} , K_S and G_S , can be found in Kotsovos and Pavlovic (1995).

Since σ_{id} is a pure hydrostatic correction, the expressions in Eqs. (28) are equivalent to the following relations which are written in the global coordinate system

$$\varepsilon_{ij} = \frac{\sigma_{ij} + \sigma_{id}\delta_{ij}}{2G_S} - \frac{3\nu_S}{E_S}(\sigma_0 + \sigma_{id})\delta_{ij} \quad (29)$$

where $E_S(\sigma_0, \tau_0, f_c)$ and $\nu_S(\sigma_0, \tau_0, f_c)$ are secant Young's modulus and Poisson's ratio derived from K_S and G_S , using the standard expressions of linear elasticity

$$E_S = \frac{9K_S G_S}{3K_S + G_S}, \quad \nu_S = \frac{3K_S - 2G_S}{6K_S + 2G_S} \quad (30)$$

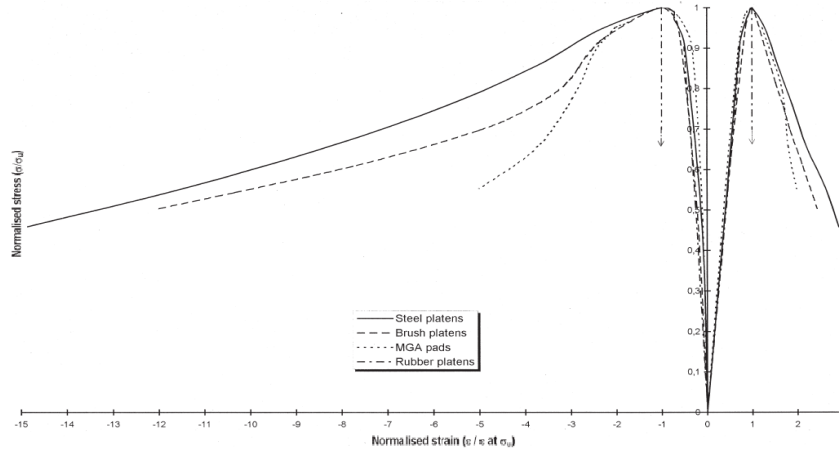


Fig. 16 Stress-strain curves for different types of boundary conditions of the experimental setup (van Mier *et al.* 1997)

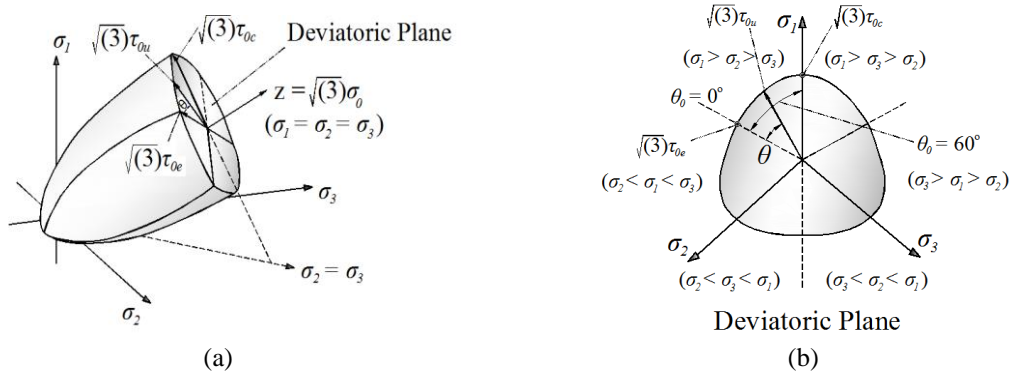


Fig. 17 Schematic representation of the ultimate-strength surface. (a) General view in stress space; (b) Typical cross-section of the strength envelope coinciding with a deviatoric plane

The nonlinear deformation component of concrete corresponding to τ_0 is considerably larger than that for σ_0 (Kotsovos 1984) and if $max \tau_0$ corresponds to the maximum deviatoric stress at each point on the stress-strain curve, then the elastic unloading/reloading occurs whenever the deviatoric stress τ_0 becomes less than $max \tau_0$.

3.2 Failure criteria

The octahedral stresses are used to describe the failure of the concrete, which may be represented in the three-dimensional principal stress space by an open and convex failure surface. The projection of the failure surface on the deviatoric plane, which is normal to σ_0 , results in a curve that represents the geometric locus of the ultimate deviatoric stress τ_{0u} (Kotsovos and Pavlovic 1995). This ultimate stress may be calculated from σ_0 and θ , where θ is the rotational angle that the deviatoric stress vector forms with one of the projected stress principal axes on the deviatoric plane

$$\tau_{0u} = \frac{2\tau_{0c}(\tau_{0c}^2 - \tau_{0e}^2)\cos\theta + \tau_{0c}(2\tau_{0e} - \tau_{0c})\sqrt{4(\tau_{0c}^2 - \tau_{0e}^2)\cos^2\theta + 5\tau_{0e}^2 - 4\tau_{0c}\tau_{0e}}}{4(\tau_{0c}^2 - \tau_{0e}^2)\cos^2\theta + (\tau_{0c} - 2\tau_{0e})^2} \quad (31)$$

This expression describes a smooth convex curve with tangents perpendicular to the directions of τ_{0e} and τ_{0c} at $\theta = 0^\circ$ and $\theta = 60^\circ$, respectively (Fig. 17). Therefore, a full description of the strength surface can be established when the variants of σ_0 , τ_{0e} , and τ_{0c} are determined. A mathematical description of the two strength envelopes may be obtained as previously, by fitting curves to the experimental data.

3.3 A modified concrete material model

3D concrete material models combined with the smeared crack approach, introduce numerical instabilities to the NR iterative procedure particularly when the RC reinforcement begins to yield. In some cases non-convergence or divergence of the nonlinear solution was observed when cracking develops locally, thus the structure appears to fail prematurely without entering the failure zone. This is the result of an instability introduced through the constitutive matrix \mathbf{C} (Eqs. 33-34) where eventually several diagonal terms of the elemental stiffness matrix take zero or near to zero values. Furthermore, when the opening of cracks occurs, abrupt unbalanced forces are developed which induce instability in the solution algorithm especially when a large number of cracks open simultaneously.

In the numerical studies performed by Kotsovos and Pavlovic 1995 they used 20- and 27-node hexahedral elements with a $3 \times 3 \times 3$ integration rule. They encountered serious convergence problems which led them to introduce a restriction on the maximum number of cracks (2 or 3) that were allowed to open at each NR iteration, in an effort to overcome convergence problems. This artificial control of crack opening impaired the robustness of the numerical formulation as different values for the restriction parameter led to different numerical results and in several cases to an overestimation of the structural strength. The effect of this restriction is illustrated in Fig. 18 where the load-deflection curve is shown for a simply supported beam without stirrups (Bresel and Scordelis 1963). The resulting curves exhibit different inelastic branches and ultimate load capacities underlying the weakness of this restriction.

Spiliopoulos and Lykidis 2006, managed to overcome this problem by allowing all cracks to occur at any Gauss point when the corresponding deviatoric stress strength is reached. This treatment required the implementation of 27-noded elements with a corresponding $3 \times 3 \times 3$ integration rule which led to an increased computational effort. Contrary to the previous implementations, an 8-noded hexahedral element with a $2 \times 2 \times 2$ integration rule, combined with a modified Kotsovos and Pavlovic material model and a unified treatment for the crack opening mechanism is used in this work. This modeling approach proves to be both stable and computationally efficient.

The Kotsovos and Pavlovic material model, assumes a nonlinear behavior for the moduli K_S and G_S for very low values of $\tau_{0u} \ll \max \tau$. The updating of the hexahedral stiffness matrices, at the early stages of loading, demands extra computational effort with no measured effect on the structural behavior. Thus, in the Kotsovos and Pavlovic material model formulation, it is necessary

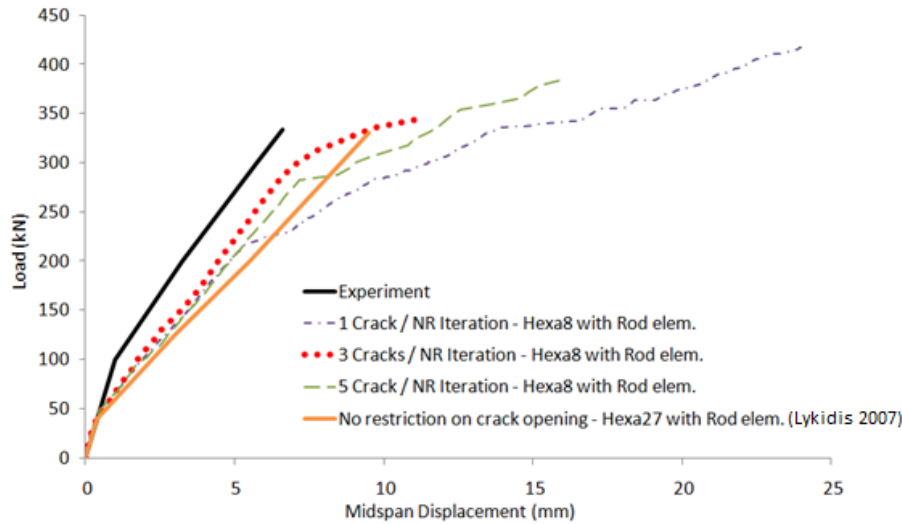


Fig. 18 Influence of the allowable number of cracks per NR iteration with the material models proposed in Kotsovos and Pavlovic 1995 and Lykidis 2007 combined with Hexa8 and Hexa27, respectively

to update the material constitutive matrix at each hexahedral Gauss point according to the change of K_S and G_S moduli. Having to solve an ill-posed numerical problem when cracking occurs, the uncracked hexahedral elements induce additional numerical instability, as a result of the unbalanced forces produced due to the update of the material constitutive matrix. This increases the computational cost due to the requirement for a continuous stiffness update.

Taking into consideration these numerical difficulties, which were also confirmed through the work performed by Papanikolopoulos 2003, a modification to the numerical handling of the Kotsovos and Pavlovic material model is proposed. Following a parametric investigation it was concluded that if the ultimate deviatoric stress τ_{0u} at any Gauss point is less than 50% of the corresponding ultimate strength (Eq. 31), then the elastic constitutive matrix \mathbf{C} can be retained in the formulation of the stiffness matrix. It is only when the deviatoric stress τ_{0u} exceeds 50% of the corresponding ultimate strength, that the nonlinear material law is activated and the constitutive matrix is computed by updating the K_T and G_T moduli. Fig. 19 illustrates the flow chart of the proposed numerical handling of the material model. This assumption can be justified from Fig. 16 which illustrates different stress-strain curves that resulted from typical compressive tests of cylindrical concrete specimens (van Mier 1997). One can easily notice that for all experiments, the slope of these curves is almost constant until compression reaches the vicinity of the failure load. The above assumption is also going to be confirmed in the section of numerical examples.

3.4 Smearred crack modeling

Smearred crack models take into consideration crack openings by modifying the calculation of stiffness matrices and stresses at corresponding integration points. This approach proceeds with the simulation of individual cracks without the need for remeshing, as it is required for the case of the discrete-crack approach where a physical gap in the FE mesh is introduced at the location of the

crack.

The smeared crack model implemented in this work is based on the work of Rashid 1968 as described by Gonzalez-Vidosa *et al.* 1991. In the framework of an incremental iterative procedure the increments of stresses at each Gauss point are found from the increments of strains through the constitutive matrix C .

$$\Delta\sigma = C \cdot \Delta\varepsilon \tag{32}$$

A crack occurs when the ultimate deviatoric stress τ_{0u} at a Gauss point has been exceeded (usually in tension or in combination of tension and compression). Then a plane is formed (crack's plane) which is perpendicular to the direction of the maximum tensile stress that exists before cracking. This tensile stress is set to zero inducing unbalanced forces at the element nodes. The incremental stress-strain relation of Eq. (32) is transformed to the corresponding Cartesian axes (x' , y' , z') of the crack before properly adjusted to take into consideration zero stress along the perpendicular axis to the plane of crack (*axis* z') and a modified shear rigidity G along the plane of crack

$$\begin{Bmatrix} \Delta\sigma'_x \\ \Delta\sigma'_y \\ \Delta\sigma'_z \\ \Delta\tau'_{xy} \\ \Delta\tau'_{yz} \\ \Delta\tau'_{zx} \end{Bmatrix} = \begin{bmatrix} 2G + \mu & \mu & \cdot & \cdot & \cdot & \cdot \\ \mu & 2G + \mu & \cdot & \cdot & \cdot & \cdot \\ \cdot & \cdot & \cdot & \cdot & \cdot & \cdot \\ \cdot & \cdot & \cdot & G & \cdot & \cdot \\ \cdot & \cdot & \cdot & \cdot & \beta G & \cdot \\ \cdot & \cdot & \cdot & \cdot & \cdot & \beta G \end{bmatrix} \cdot \begin{Bmatrix} \Delta\varepsilon'_x \\ \Delta\varepsilon'_y \\ \Delta\varepsilon'_z \\ \Delta\gamma'_{xy} \\ \Delta\gamma'_{yz} \\ \Delta\gamma'_{zx} \end{Bmatrix} \tag{33}$$

where μ is the Lamé constant. A schematic representation of the planes of cracks and the corresponding axis is depicted in Fig. 20.

Following this crack formulation, if a tensile state of stress is reached in a different direction at a subsequent load level, then a second crack opens with its corresponding plane being perpendicular to the direction of the new maximum principal tensile stress. Hence, in combination with the previous state of stress, non-zero stress can only be developed along the intersection of the two planes (Fig. 20). Consequently, the incremental stress – strain relations along these Cartesian axes (x'' , y'' , z'') are given by

$$\begin{Bmatrix} \Delta\sigma''_x \\ \Delta\sigma''_y \\ \Delta\sigma''_z \\ \Delta\tau''_{xy} \\ \Delta\tau''_{yz} \\ \Delta\tau''_{zx} \end{Bmatrix} = \begin{bmatrix} \cdot & \cdot & \cdot & \cdot & \cdot & \cdot \\ \cdot & 2G + \mu & \cdot & \cdot & \cdot & \cdot \\ \cdot & \cdot & \cdot & \cdot & \cdot & \cdot \\ \cdot & \cdot & \cdot & \beta G & \cdot & \cdot \\ \cdot & \cdot & \cdot & \cdot & \beta G & \cdot \\ \cdot & \cdot & \cdot & \cdot & \cdot & \beta G \end{bmatrix} \cdot \begin{Bmatrix} \Delta\varepsilon''_x \\ \Delta\varepsilon''_y \\ \Delta\varepsilon''_z \\ \Delta\gamma''_{xy} \\ \Delta\gamma''_{yz} \\ \Delta\gamma''_{zx} \end{Bmatrix} \tag{34}$$

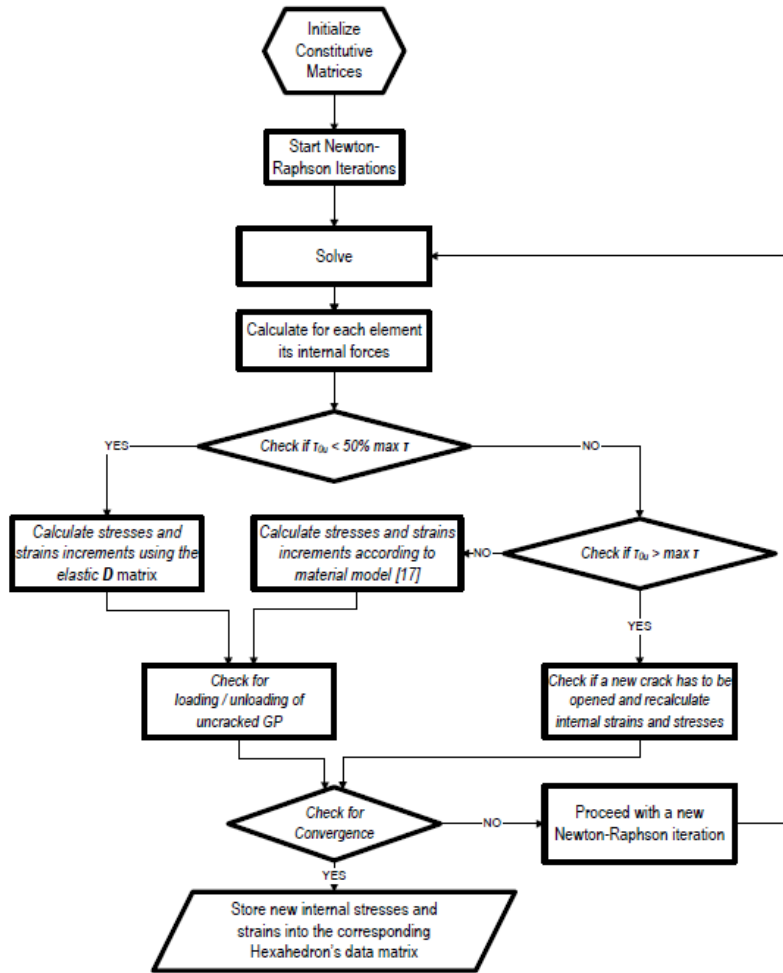


Fig. 19 Flow chart of the adopted concrete material model

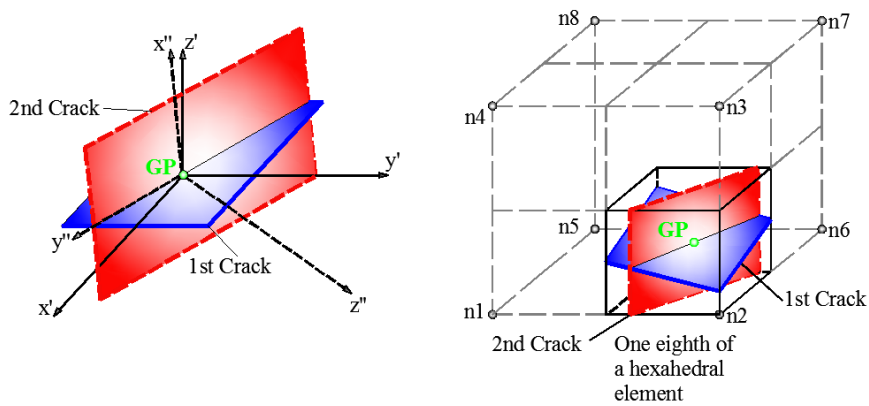


Fig. 20 Local axes for the case of two cracks at a specific Gauss point

In the event that a third tensile stress occurs in a different direction at the same Gauss point, then a zero stiffness contribution is assumed for this specific Gauss point.

Parameter β plays an important role in most cases, when using the smeared crack approach, as a result of its contribution to the stability of the nonlinear iterative procedure when cracks open. If this parameter is set to zero with the creation of a crack, then zero diagonal terms may appear in the global stiffness matrix, particularly when the RC structure is sparsely reinforced. The physical meaning of this parameter is related to the remaining stiffness due to aggregate interlocking along the cracks surface. An acceptable value for this variable is $\beta = 0.1$ which was extracted from experimental data (Kotsovos and Pavlovic 1995, Gonzalez-Vidoso 1988). This implies that 10% of the initial shear strength is remaining after the opening of the crack as a result of the aggregate interlocking along the crack's plane.

4. Numerical experiments

4.1 RC beams with and without stirrups

With these two numerical experiments, we will try to illustrate the importance of taking under consideration the stiffness of reinforcement by treating the rebars as beam elements instead of rod elements. The computational efficiency of the numerical treatment of the proposed formulation will also be demonstrated through the following numerical tests.

4.1.1 RC beam without stirrups under central point load

The first numerical experiment consists of a simply supported beam with no stirrups (Bresler and Scordelis 1963). Its geometrical features are depicted in Fig. 21. The experimental failure load was reported to be equal to 334kN with a corresponding central deflection of 6.6 mm. Fig. 22 shows the first FE model which consists of 132 hexahedral elements for concrete and 88 *NBCFB* elements for the embedded reinforcement. Furthermore, two additional denser meshes were created, containing 264 and 528 hexahedral concrete elements (Fig. 23) in order to investigate the mesh sensitivity of the proposed method.

The four longitudinal bars have a diameter of 28.9 mm which represents a large reinforcement ratio (1.52%) corresponding to the beam sectional dimensions (309.9 mm width and 556.3 mm height). The results obtained for different simulations are shown in Fig. 24.

Curves 8 and 9 in Fig. 24 were obtained using 27-noded and 8-noded hexahedral elements, respectively, rod elements for the embedded reinforcement and the Kotsovos and Pavlovic concrete material model. As can be seen, both formulations managed to predict the ultimate load exhibiting a markedly softening behavior compared to the experimental one. On the other hand, the curves obtained by the ATENA commercial software (Curves 2-4), follow closely the experimental curve but appear to underestimate considerably the ultimate load of the beam. These differences cannot be attributed to the different concrete material model used in ATENA, which is based on the cubic compressive strength instead of the cylindrical, since the bearing capacity is well under estimated corresponding to the experimental results. Curves 5, 6 and 7 were obtained with the present formulation showing a very good agreement with the experimental results. In all tests performed perfect-bond of the rebars is assumed. The predicted failure loads and the corresponding mid-span deflections are shown in Table 1. The predicted values illustrate the

numerical accuracy of the proposed method and its robustness with respect to different meshes. The failure of the beam was initiated due to cracking of the beam compressive zone, as can be seen in Fig. 25, where the deformed shape and crack pattern of the beam prior to failure are illustrated.

A breakdown of the required computational effort for the 132 Hexa8 elements model is shown in Table 2, where it can be seen that the required CPU time for solving this nonlinear problem with 30 load increments was 7 seconds.

The required computational effort of ATENA software was approximately 9 minutes for the nonlinear solution when using 132 Hexa8 elements, 24 minutes for the case of 264 Hexa8 elements and 50 minutes for the case of 528 Hexa8 elements (Table 1). It has to be mentioned that ATENA performs several graphical representation procedures during execution, which are incorporated into the nonlinear CPU solution time.

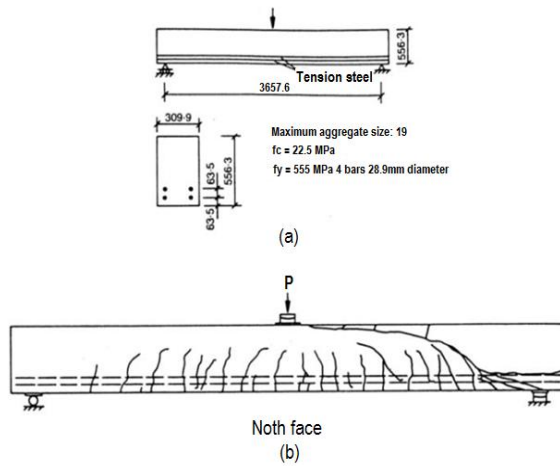


Fig. 210 RC beam without stirrups under central point load. (a) Beam characteristics, b) experimentally observed crack pattern at ultimate load (Bresler and Scordelis 1963)

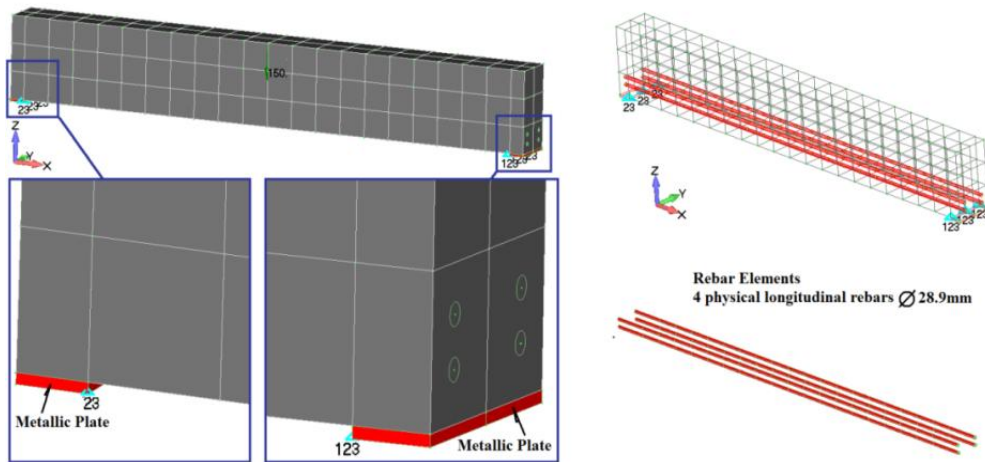


Fig. 22 Beam without stirrups under central loading. FE mesh

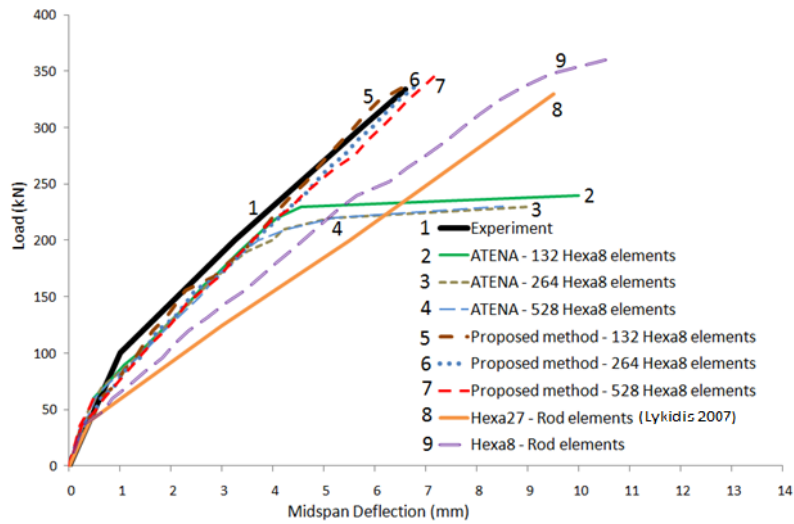


Fig. 24 RC beam without stirrups under central point load. Predicted and experimental load-midspan deflection curves for different FE models

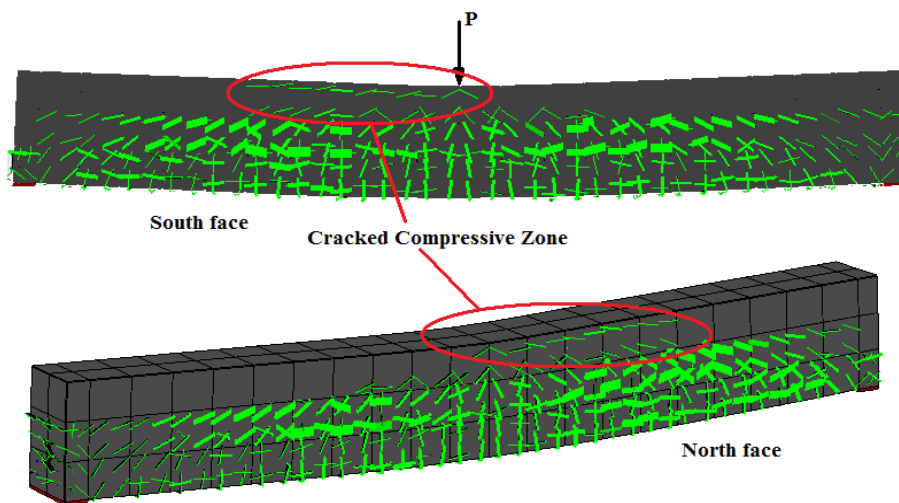


Fig. 25 RC beam without stirrups with 132 Hexa8 elements under central point load. Crack pattern and deformed shape prior to failure

Table 3 shows the required number of NR iterations during the solution procedure for the beam without stirrups for the case of 132 Hexa8 concrete elements. It can be seen that most of the load steps when using the proposed modeling method, require less than 6-8NR iterations. However, in some load steps, like the 10th load step, an increased number of internal iterations is required due to the large number of crack openings. In Fig. 26 the crack patterns at load steps 9 and 10 are

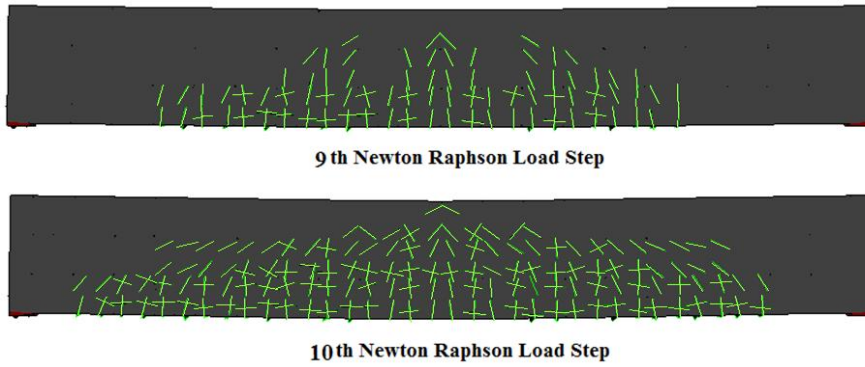


Fig. 26 RC beam without stirrups with 132 Hexa8 elements under central point load. Crack pattern at the 9th and 10th load increments

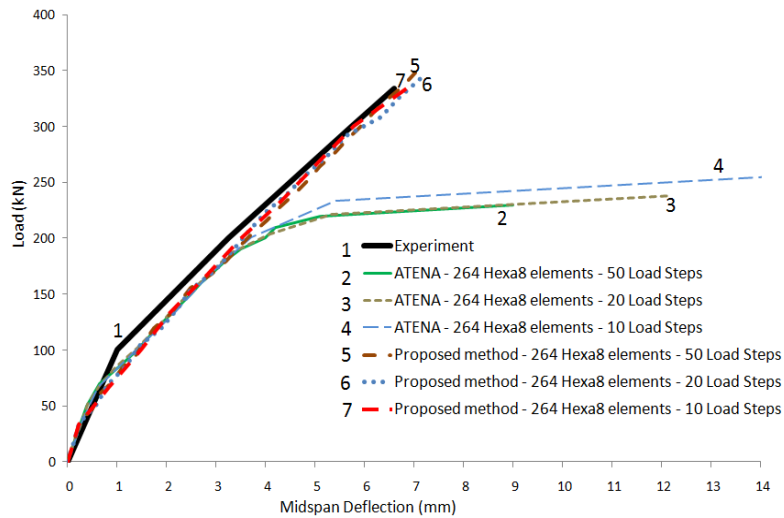


Fig. 27 RC beam without stirrups with 264 Hexa8 elements under central point load. Load-deflection curves for different load increments

Table 1 RC beam without stirrups under central point load. Predicted failure load, mid-span deflections and CPU solution time for different meshes

<i>Model</i>	<i>Failure Load (kN)</i>	<i>Deflection (mm)</i>	<i>Load Increments</i>	<i>CPU time (sec)</i>
Proposed method – 132 Hexa8 elements	338	6.7	30	7
Proposed method – 264 Hexa8 elements	348	7.0	30	18
Proposed method – 528 Hexa8 elements	348	7.2	30	55
ATENA – 132 Hexa8 elements	240	>8	24	540
ATENA – 264 Hexa8 elements	230	>8	23	1440
ATENA – 528 Hexa8 elements	230	>8	23	3000

Table 2 RC beam without stirrups with 132 Hexa8 elements under central point load. CPU time for different tasks of the nonlinear analysis

<i>Task</i>	<i>CPU Time (sec)</i>
Embedded Rebar Element Mesh Generation	0.02
Newton-Raphson Non Linear Solution	7.00
Writing Output Data	12.00
Other	0.08
<i>Total Time</i>	20.0

Table 3 RC beam without stirrups with 132 Hexa8 elements under central point load. NR iterations per load step

<i>Newton-Raphson Iterations per load step</i>	
<i>ATENA</i>	1 1 1 1 8 12 23 21 18 8 17 14 8 14 9 17 40 12 15 40
<i>Proposed Method</i>	1 1 1 4 6 3 8 3 1 14 1 2 11 15 2 6 5 4 3 2 6 2 2 4 3 6 4 3 2 18

Table 4. RC Beam without stirrups with 264 Hexa8 elements under central point load. CPU time until failure for different load increments

<i>Load Increments</i>	<i>CPU Time (sec)</i>
50	25
20	17
10	11

depicted illustrating the additional cracks that were created in a single load step which explains the increased number of iterations at this step.

In order to illustrate the computational efficiency of the proposed modeling method, different loading increments are applied for the case of 264 Hexa8 element discretization and the corresponding load-deflection curves are depicted in Fig. 27. It can be seen that the variation of the predicted curves is insignificant and it can therefore be concluded that the accuracy of the solution procedure is not sensitive to the size of load increment, which is a crucial numerical property when dealing with large scale problems. The corresponding required CPU time until failure for different load increments is given in Table 4.

4.1.2 RC beam with stirrups under central point load

The second numerical test refers to the same beam specimen with stirrups and compression reinforcement, as shown in Fig. 28. Local stiffening is applied in the experimental set-up in the region of the central point load and at the support regions. The collapse of this beam member occurred when the central point load reached 467kN with a corresponding mid-span deflection of 13.8 mm (Bresler and Scordelis 1963). The failure of the beam was brittle without yielding of the

tension bars. Diagonal cracking began at the same load level as for the beam without stirrups (267kN), but did not lead to failure due to the presence of stirrups and compression reinforcement. Fig. 29 shows the FE model that was used for this numerical experiment which consists of 102 hexahedral elements for concrete and 354 *NBCFB* elements for the embedded reinforcement.

As can be seen from Fig. 30, the predicted failure load of the proposed modeling is equal to 448kN with a corresponding midspan deflection of 13.5 mm for the case where the external load is divided into 50 load steps (Curve 4). Similar failure loads were also obtained for 100 and 20 load step increments (Curves 3, 4 and 5). Curve 7 shows that ATENA with rod elements for the reinforcement failed prematurely due to extensive cracking.

Fig. 31 shows the crack pattern for several load levels up to failure. Cracking in the beam's compressive zone starts for a total applied load of 300kN, but does not lead to failure of the beam due to stirrups confinement and the compressive contribution of the upper reinforcement. The numerical solution terminates when failure of the compressive bars is manifested which is in good agreement with the experimental mode of failure.

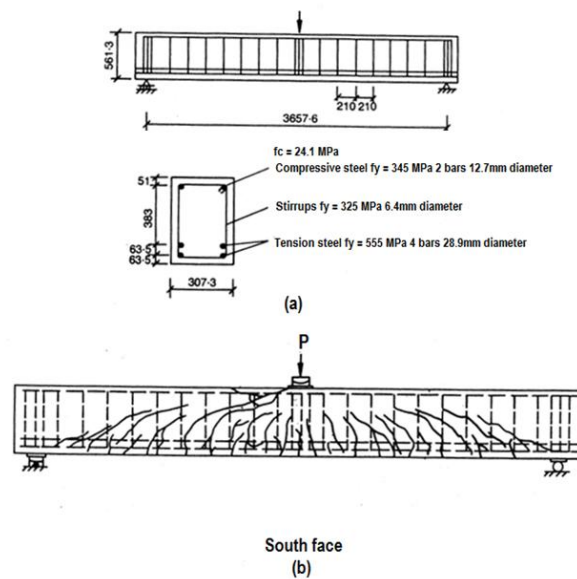


Fig. 28 RC beam with stirrups under central point load. (a) Beam characteristics and (b) experimentally observed crack pattern at ultimate load (Bresler and Scordelis 1963)

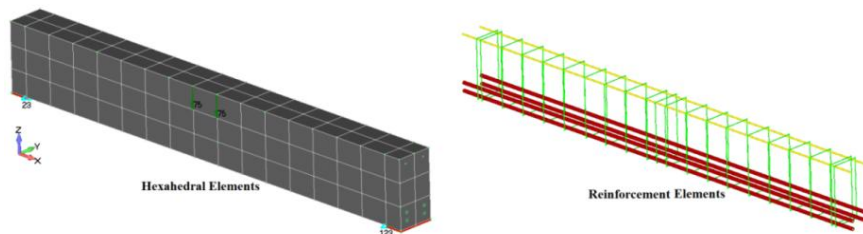


Fig. 29 RC beam with stirrups under central loading. FE model

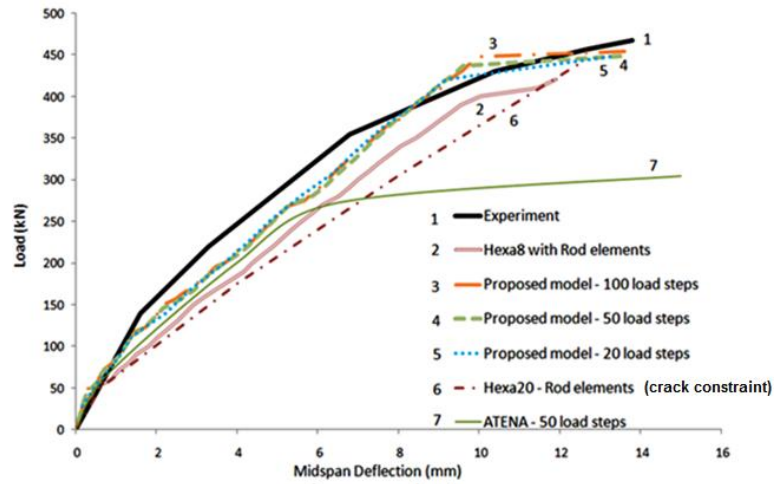


Fig. 30 RC beam with stirrups under central loading. Load-deflection curves for different FE models and load increments

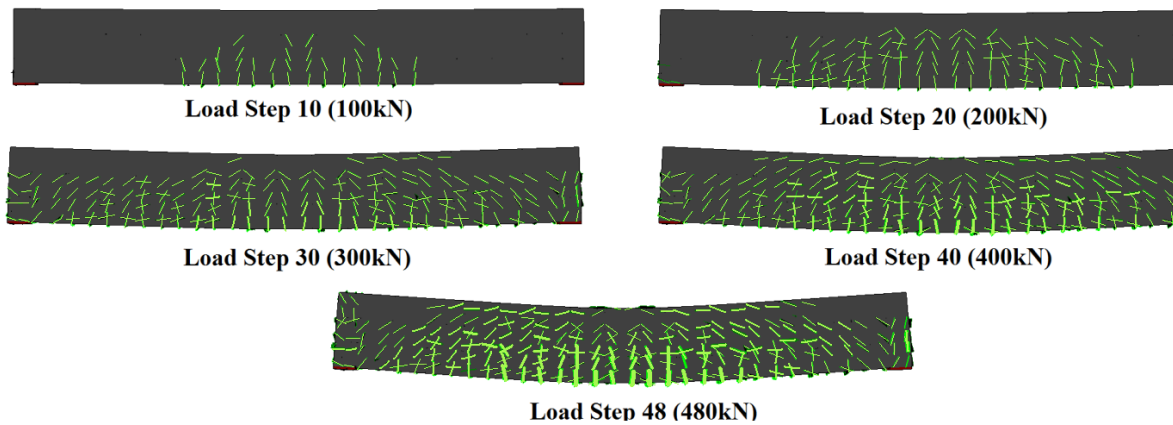


Fig. 31 RC beam with stirrups under central point load. Crack patterns and corresponding deformed shapes at different load levels

Table 5 RC beam with stirrups under central point load. CPU time for different tasks of the nonlinear analysis

<i>Task</i>	<i>CPU Time (sec)</i>
Embedded rebar element mesh generation	0.03
Nonlinear incremental-iterative solution	17.00
Writing output data	25.00
Other	0.43
<i>Total Time</i>	42.46

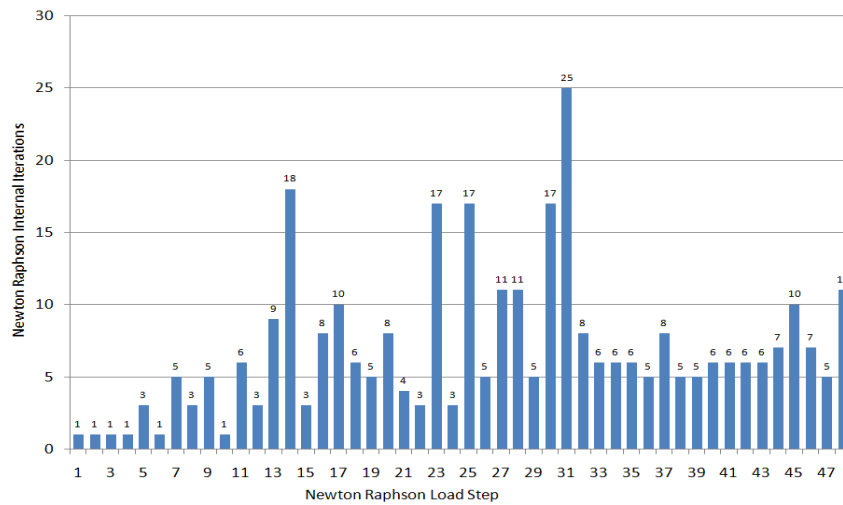


Fig. 32 RC beam with stirrups under central point load. Required NR iterations per load step

The required NR iterations for this numerical experiment are depicted in the graph of Fig. 32 for 48 load steps. The maximum required number of NR iterations occurs at load step 31 where the initiation of the compressive zone cracking takes place and crack opening is extensive due to the excessive stress redistribution.

The required computational time for the nonlinear solution procedure is depicted in Table 5 which refers to 48 incremental load steps. It can be seen that the average CPU time per load increment is 0.354 seconds compared to 0.177 seconds for the corresponding problem without stirrups. This is attributed to the fourfold increase of the number of rebar beam elements used for this discretization. The corresponding computational time when analyzing this model with ATENA software for 25 steps was 15 minutes.

4.2 RC shear wall

Lefas (1988) and Lefas and Kotsovos (1990) conducted experimental studies on RC shear walls with different geometric characteristics and reinforcement arrangements. The geometric details of the shear wall denoted as Type I are given in Fig. 33. The walls were monolithically connected at their ends to two beams. The lower beam was utilized to clamp down the specimens to the laboratory test floor.

The reinforcement used in these RC shear walls consisted of two different diameters and yielding stresses (Table 6). Both of them were high tensile strength rebars of 8 mm and 6.25 mm in diameter. In addition to the longitudinal reinforcement, horizontal stirrups were placed at the edges of the walls (concealed columns) providing confinement. Mild rebars of 4mm diameter were used for this purpose.

The shear wall specimens were clamped to the floor by means of two transverse long steel box girders 10 mm thick and 4 holding-down post tensioned bolts. As it can be seen from Fig. 34, the vertical constant load was applied through a two point loading.

The specimens were designed based on the 1983 edition of the ACI code. All specimens have the same reinforcement but were loaded with a different load combination. Three different vertical

loads were used: 0 , $0.1 \cdot A \cdot f_c$ and $0.2 \cdot A \cdot f_c$ where A and f_c are the shear wall sectional area and cylindrical concrete compressive strength, respectively. Table 7 and Fig. 35 contain information associated with the reinforcement detailing and the level of constant vertical load applied for the three specimens denoted as SW14, SW15 and SW16, the level of maximum horizontal load attained during the experimental testing, as well as the different concrete compressive strength and loading history. The same FE mesh, shown in Fig. 36, is used for modeling the three specimens. The FE mesh consists of 96 hexahedral elements and 949 embedded rebar elements. The predicted numerical curves by the proposed modeling are compared with the corresponding experimental curves in Fig. 37 where a satisfactory correlation can be observed. It is worth mentioning here that the sudden increase of displacements observed in Fig. 37a is attributed to the abrupt loss of stiffness as a result of crack opening associated with the smeared crack approach.

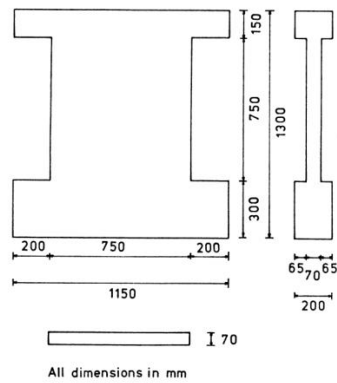


Fig. 33 Shear wall specimen (Lefas 1988)

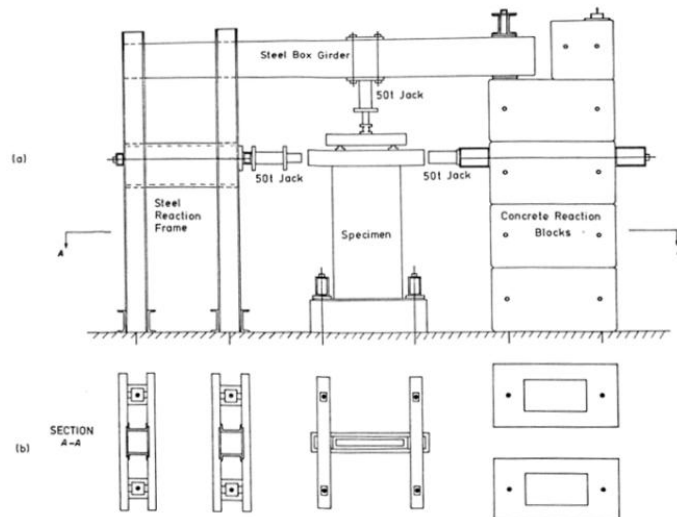


Fig. 34 RC shear wall. Schematic representation of the test rig. (a) Elevation; (b) plan view (Lefas 1988)

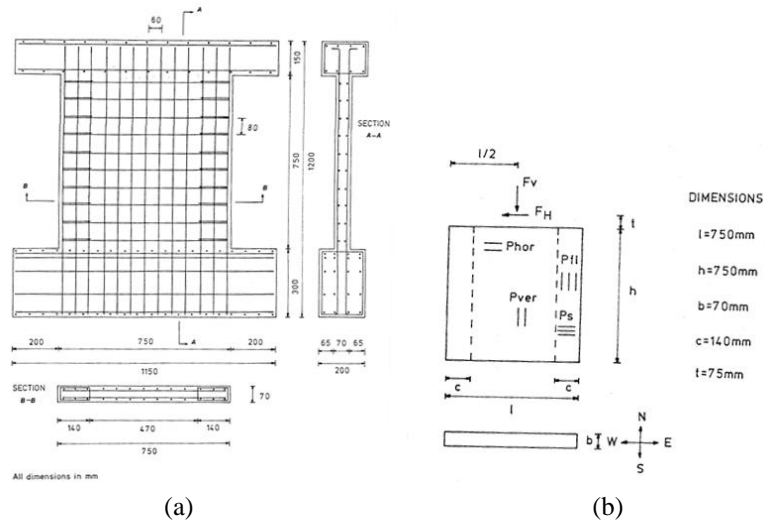


Fig. 35 Shear wall. Reinforcement details (Lefas 1988)

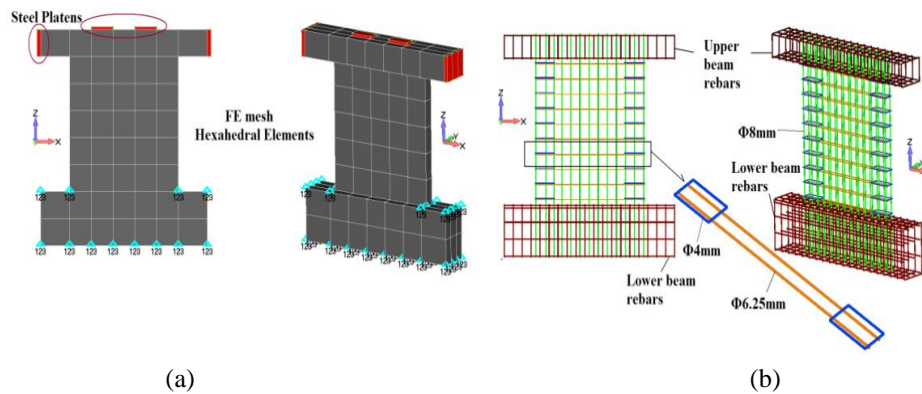


Fig. 36 Shear wall. 2D and 3D views of the FE mesh. (a) Hexa8 elements; (b) Reinforcement rebar

The crack patterns at the failure load are depicted in Figs. 38 and 39. The largest cracks appear to be the flexural cracks that are located on the base of the three specimens where the RC shear walls are connected to the lower beam. Fig. 39 shows the three characteristic crack patterns that were predicted with the proposed method and were also measured by Lefas 1988 for the case of SW14. The corresponding experimental values for the three numerical cases are given in Table 8 where the good agreement between experimental and analytical data can be verified. The initiation of inclined cracking for SW14 was reported to occur for a corresponding load of 100kN which is close to the numerically obtained value (87kN). The CPU time required for the solution of the three numerical models are given in Table 9. The variation of the computational effort is attributed to the different NR iterations required at each load increment. For the case of specimen SW15 a larger number of NR iterations per load increment was required due to an increased rate of crack openings which explains the difference in the CPU time.

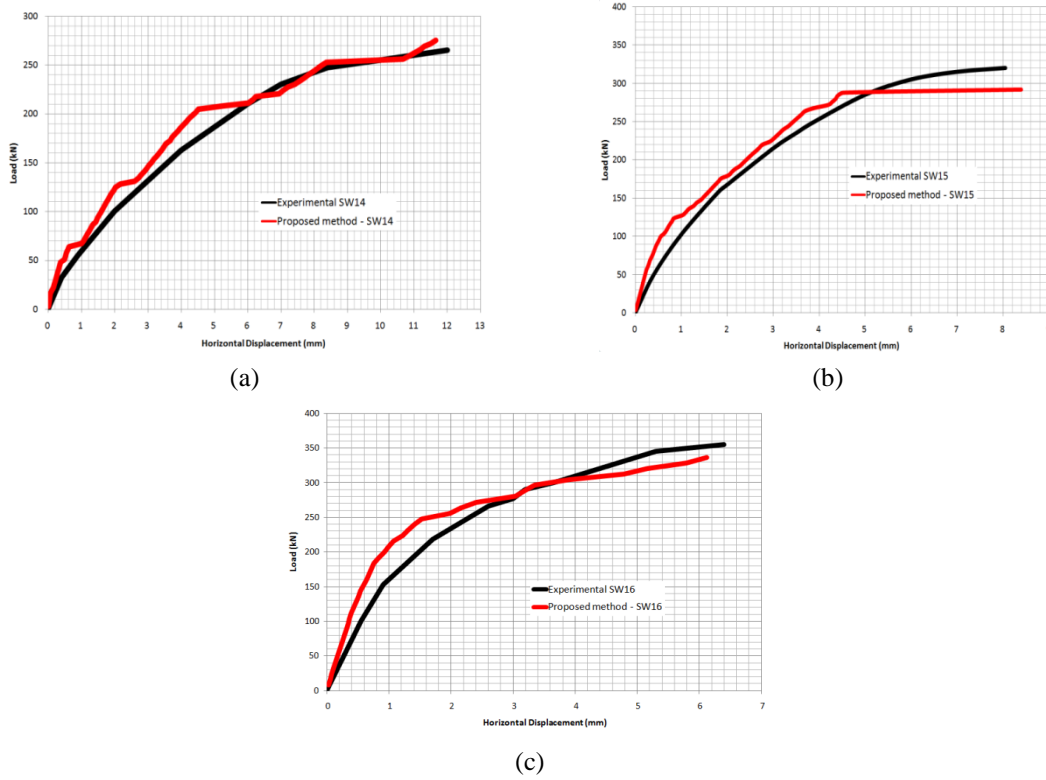


Fig. 37 Shear wall. Experimental and predicted curves for the three specimens: (a) SW14; (b) SW15 and (c) SW16

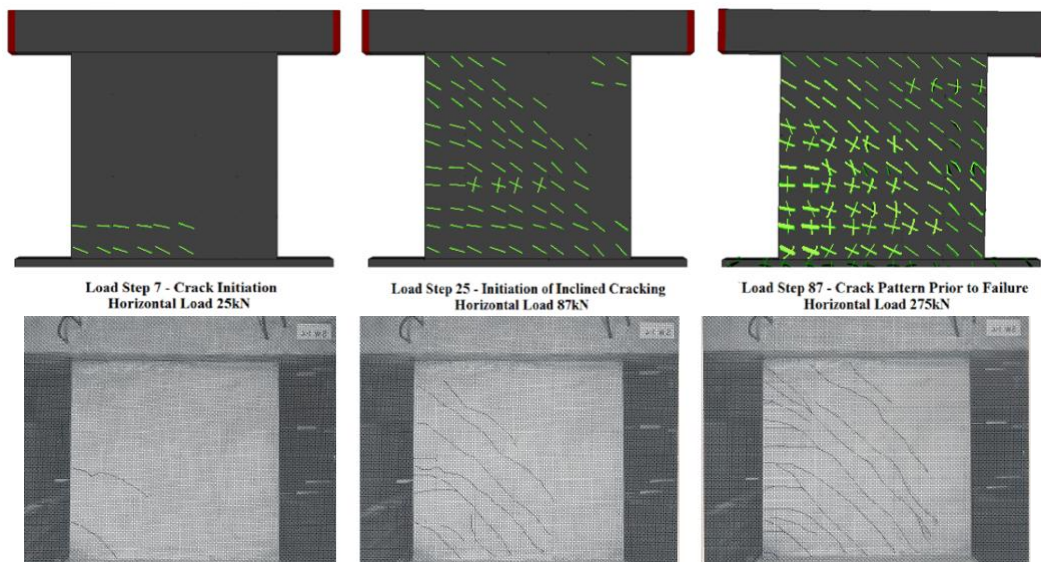


Fig. 38 Shear wall. Predicted and experimentally observed crack pattern for different load levels of specimen SW14

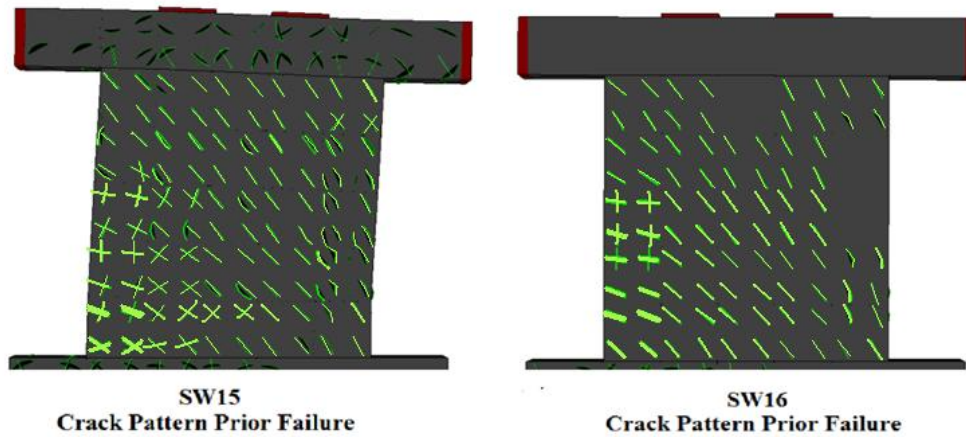


Fig. 39 Shear wall. Predicted crack pattern of specimens SW15 and SW16 at ultimate loads

Table 6 Material properties of the reinforcement used for the RC shear walls

Steel Bar Type	Yield strength f_{sy} (MPa)	Ultimate strength f_{su} (MPa)	Modulus of elasticity E_s (GPa)
8 mm - high tensile bar	470	565	159
6.25 mm - high tensile bar	520	610	150
4 mm - mild steel bar	420	490	-

Table 7 Shear wall. Reinforcement percentage, load data and concrete strength for three specimens (Lefas 1988)

Specimen	Reinforcement Percentage				Vertical Load		Ultimate Horizontal Load	Concrete's Cylinder Strength
	P_{hor} (%)	P_{ver} (%)	P_{fl} (%)	P_s (%)	F_v (kN)	$\frac{F_v}{b l f_c}$	F_H (kN)	f_c (MPa)
SW14	1.1	2.4	3.1	1.2	0	0	265	34.0
SW15	1.1	2.4	3.1	1.2	185	0.10	320	30.5
SW16	1.1	2.4	3.1	1.2	460	0.20	355	43.6

Table 8 Shear wall. Predicted initiation of cracking and ultimate horizontal loading

Specimen	Initiation of Cracking – Predicted Data		Initiation of Cracking – Experimental Data		Ultimate Horizontal Load - Predicted	Ultimate Horizontal Load - Experimental
	F_H (kN)	δ (mm)	F_H (kN)	δ (mm)	F_U (kN)	F_U (kN)
SW14	35	0.34	25	0.25	275.5	265
SW15	45	0.27	59	0.22	304.5	320
SW16	80	0.40	80	0.31	336	355

Table 9 Shear wall. CPU time for the nonlinear solution procedure

<i>a/a</i>	<i>Specimen</i>	<i>Load Increments</i>	<i>CPU Time (sec)</i>
1	SW14	86	50
2	SW15	87	60
3	SW16	88	35

4.3 RC Shear panel beam

The shear panel beam W-2 tested by Červenka 1970 has been frequently used by many researchers (Lykidis 2007, Ile and Reynouard 2000, Kwak and Kim 2004, Darwin and Pecknold 1976, Kwak and Kim 2001) in order to verify their numerical models. The panel beam consists of two orthogonally reinforced panels, 762 mm wide, 762 mm high and 76.2 mm thick, separated by three ribs (Fig. 40). The concrete's compressive strength was $f_c = 26.8$ MPa and the reinforcement steel material properties were $E_s = 190$ GPa and $f_y = 353$ MPa. The experimental findings showed that the ultimate load capacity of this panel beam is governed by yielding of the reinforcing steel following initial tensile cracking of concrete. Ultimately, the panel beam failed by local concrete crushing and splitting in the compressive zone of the panel.

The finite element discretization and the corresponding reinforcement percentage are shown in Fig. 41 and Table 10, respectively. Two FE discretizations are considered for the modeling of concrete with 100 and 328 solid elements as shown in Figs. 41a and 41b. In both FE models the reinforcement geometry remains the same (Figs. 41c and 41d).

The experimental and predicted curves are shown in Fig. 42, where good agreement between the results is observed. It can be seen that the proposed numerical model manages to predict the ultimate failure load (118kN) with an acceptable accuracy while both elastic and inelastic predicted branches appear to be in good correlation with the experimental curve. When the external applied load reaches approximately 70% (80kN) of the failure load, the prediction of the RC member stiffness is overestimated. This is attributed to the stiffness introduced through the use of the β parameter when excessive cracking occurs (Fig. 43b).

Fig. 43 shows the crack patterns for both FE meshes for different load levels. It can be seen that the predicted failure mode is governed by flexural cracking which occurred at the load level of 40 kN and 35 kN for the sparse and fine FE models, respectively. The initiation of cracking occurred at a slightly lower load level for the case of the model with the fine FE mesh. For both cases the crack patterns were flexure dominated and the failure mechanism was initiated when the longitudinal reinforcement located at the basis of the specimen yielded, following the failure of the shear panel compressive zone. The computational performance of the proposed model is depicted in Table 11.

Table 10 RC Shear Panel Beam. Reinforcement percentage

<i>Region</i>	<i>Direction</i>	<i>Reinforcement Percentage</i>	
		<i>Panel</i>	<i>Ribs</i>
A	x	0.92%	0.23%
A	y	0.92%	0.47%
B	x	1.83%	0.47%
B	y	0.92%	0.47%

Table 11. RC Shear Panel Beam. CPU time for the nonlinear solution procedure

<i>a/a</i>	<i>Num. of Hexa8 Elements</i>	<i>Load Increments</i>	<i>CPU Time (sec)</i>
1	100	20	10
2	100	50	15
3	328	20	40
4	328	50	60

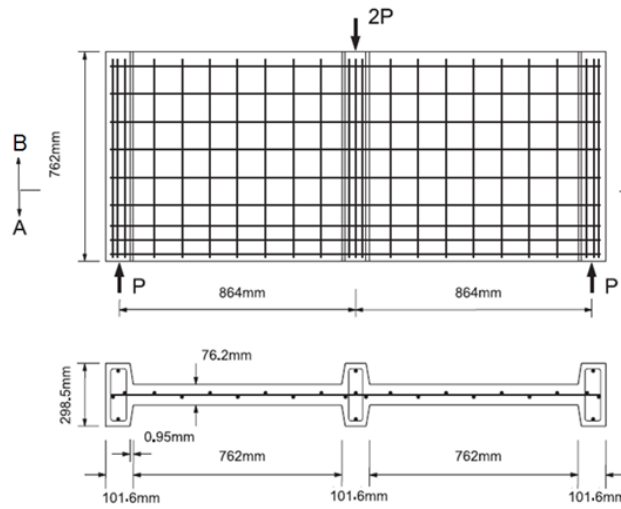


Fig. 40 RC Shear Panel Beam. Geometry and reinforcement details (Červenka 1970)

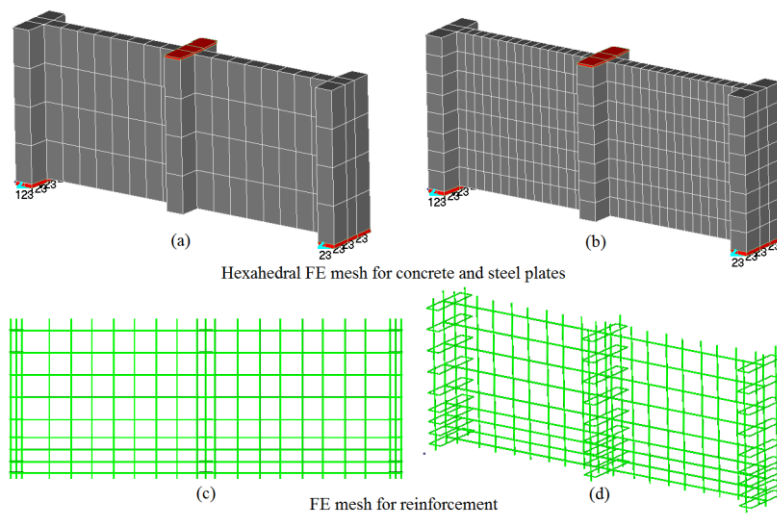


Fig. 41 RC Shear Panel Beam. FE mesh with (a) 100 and (b) 328 concrete hexahedral elements; (c) 2D and (d) 3D views of the FE mesh for the reinforcement grid

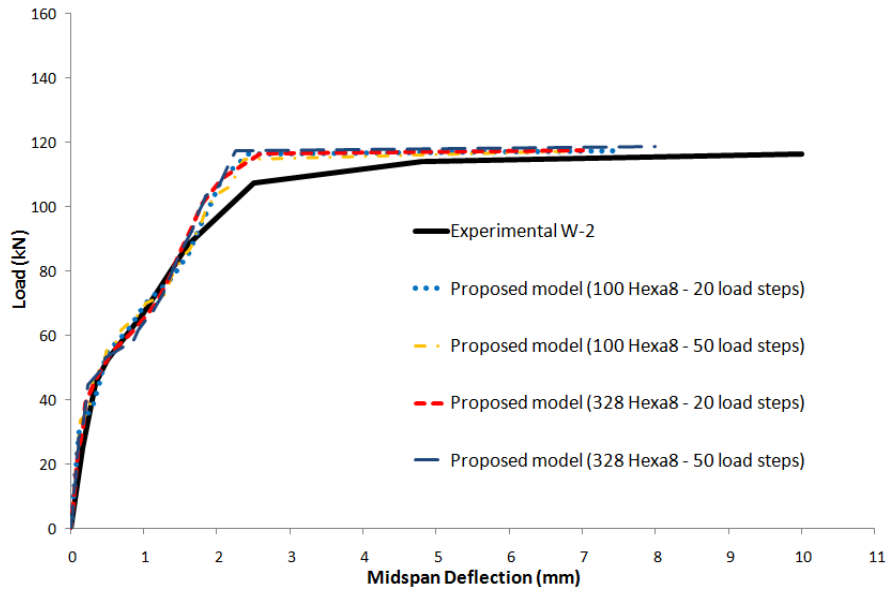


Fig. 42 RC Shear Panel Beam. Experimental and predicted curves

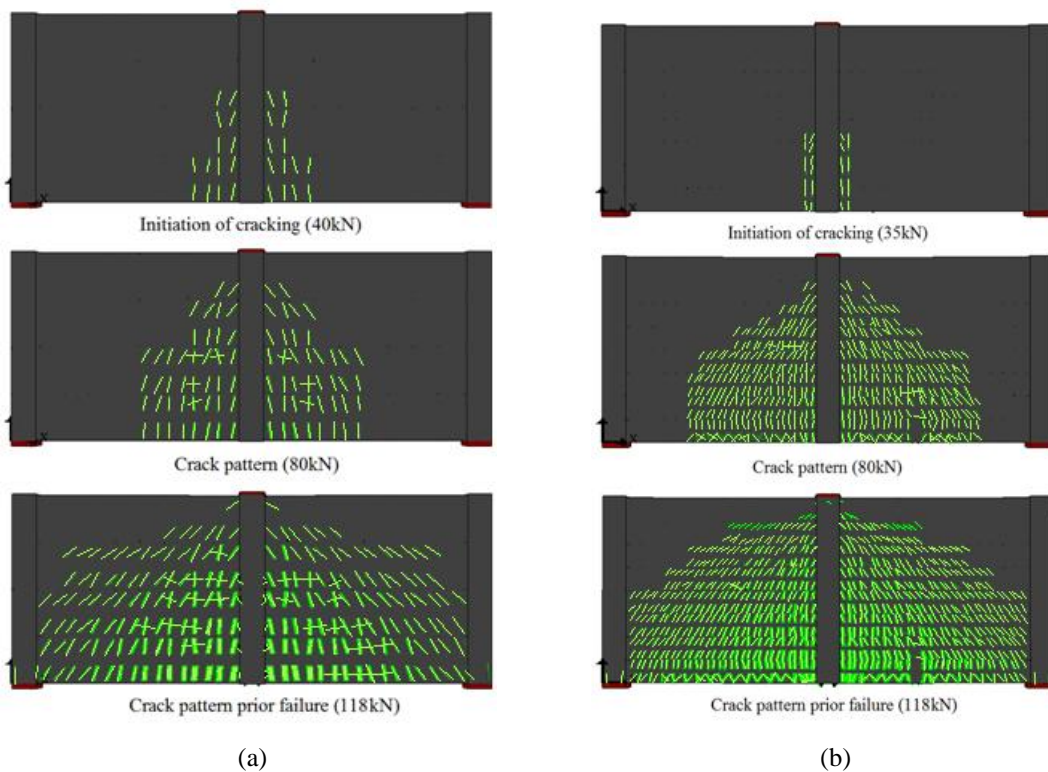


Fig. 43 RC Shear Panel Beam. Crack patterns for various load levels. (a) 100 and (b) 328 hexahedral concrete elements

5. Limitations of the proposed modeling method

The proposed modeling method uses the Kotsovos and Pavlovic material model which is presented in detail in Kotsovos and Pavlovic 1995. It is well known that this material model is not based on a thermodynamic framework in order to dissipate energy with a proper loading-reloading behavior (Bažant and Zdenek 1983). Nevertheless, its simplicity proved to be sufficient in predicting the nonlinear behavior of RC structural members (Kotsovos and Pavlovic 1995, Spiliopoulos and Lykidis 2006, Lykidis 2007, Cotsovos 2009) and promising, as illustrated in this research work, for the nonlinear analysis of full-scale RC structures. On the other hand, as Jiràsek and Rolshoven 2003 stated, in nonlocal constitutive theories the local state of the material at a given point may not be sufficient to evaluate the stress at that point. This is physically justified by the fact that no real material is an ideal continuous medium, and on a sufficiently small scale the effects of heterogeneity and discontinuity at the microstructure level become non negligible, especially for the case of highly heterogeneous composite materials, like concrete. Moreover, convergence difficulties and failure of capturing experimental results when using relatively sparse meshes make this type of models prohibitive for the analysis of full-scale RC structures. This confirms that each numerical model has its advantages and disadvantages, thus their incorporation in FE algorithms requires special handling. For an overview and discussion of various non-local plasticity formats (see Jiràsek and Rolshoven 2003).

A second limitation of the proposed modeling method is the lack of taking into account the stiffening effect and the bond-slip phenomenon. The reason for this omission is that tension stiffening effect is not usually considered with detailed 3D modeling (see all relative references of Cervera *et al.* 1987, Kotsovos and Pavlovic 1995, Ozbolt and Li 2001, Girard and Bastien 2002, Hartl and Handel 2002, Mirzabozorg and Ghaemian 2005, Spiliopoulos and Lykidis 2006, Sato and Naganuma 2007, Červenka and Papanikolaou 2008, Papanikolaou and Kappos 2009, Červenka *et al.* 2008) and since the inclusion of a bond-slip model has an opposite effect to the tension stiffening, it was decided not to consider these phenomena at this stage. In addition to that, regarding the accuracy of the proposed modeling method, the bond-slip phenomenon, plays an important role for cases where the anchorage length of the reinforcement is insufficient. When slippage occurs, near and after the yielding of the reinforcement (Viwathenatepa *et al.* 1979), it affects the elongation of the cracks' widths and the internal strain redistribution at the local regions where slippage takes place. It does not however affect the crack distribution, since crack formation takes place when reinforcement is still located in the elastic range. Nevertheless, at local level the internal redistribution of stress and strains is significantly affected near the ultimate state of the structure.

As it was illustrated above, modeling of cracking with the smeared crack approach has the disadvantage the inaccurate modeling of the physical gap of the crack and the corresponding proper stress redistribution when cracking occurs. This is attributed to the fact that the same FE mesh is used throughout the analysis procedure thus the redistribution of the released internal forces is not performed with a physically correct manner. The outcome of this numerical feature is depicted in Fig. 43a and 43b where the predicted crack patterns differ in terms of their density thus the corresponding crack widths cannot be compared. Due to the nature of the smeared crack approach, cracks appear throughout the shear panel (Fig. 43b), failing to capture the uncracked areas in between the main flexural cracks as observed in the real experiment setup. A detailed discussion on the disadvantages of the smeared crack approach can be found in Bažant and Zdenek

1983 and Bažant and Oh 1983. It is important to note that the smeared crack method appears to be for the moment the only feasible approach Oliver 1989 and Markou 2011 in modeling RC full-scale structures.

Finally, the use of parameter β after a crack opening introduces an additional stiffness in the FE model, especially in cases of flexural dominated RC structural members. Early work presented by Cedolin and Dei 1977 concluded that the shear retention factor has to be computed through an objective manner thus they proposed its connection with the crack's width. In this research work it was concluded that the crack width is not the main factor that should be considered for the activation of the shear retention stiffness. It is obvious that when a RC structural member is dominated by flexural cracks, the shear stiffness along the crack's planes should not be activated since no shear deformations are formed. Therefore, a formulation based on the stress-strain field is more appropriate for assessing whether this parameter will be activated or not and for computing its corresponding value.

It is important to note that the Kotsovos and Pavlovic material model was incorporated recently in ADINA (Bathe 1995), where a brief description of why phenomenological models are more preferable, especially when dealing with relatively large-scale models. As it is mentioned in there Tech Brief uploaded in there official website:

“There is probably no single concrete material model now available that can be universally applied, efficiently in practice, to model any concrete material and under any loading conditions (namely static, slow dynamic and fast dynamic conditions). The microstructure of concrete materials is too complex. Hence, until such model is available and finite element programs can use the model efficiently in practical large-scale analyses, it is appropriate to offer a number of concrete models in a computing environment.”

6. Conclusions

A detailed finite element modeling of reinforced concrete structures is proposed with the following characteristics:

(i) A mesh generation technique for the embedded reinforcement is implemented which can effectively allocate and generate embedded reinforcement elements inside hexahedral elements with an arbitrary positioning of the reinforcement. The objective was the reduction of the computational effort regarding the generation of the embedded reinforcement given a specific FE discretization for concrete. The computational efficiency of the proposed mesh generation method, when dealing with relatively large-scale problems with arbitrary reinforcement geometry, was shown through numerical experiments.

(ii) An improved numerical handling of a 3D material concrete model for monotonic loading combined with a smeared crack model was implemented. The material model was applied to an 8-noded hexahedral element with no restriction on the number of crack openings inside the load increment.

(iii) The modeling of the reinforcement was performed with the use of a 2-noded flexibility-based beam element, formulated with natural modes and the fiber approach. It was shown that the results obtained with rod elements for modeling the reinforcement do not lead to accurate numerical simulations especially for heavily reinforced concrete members.

(iv) The implemented *NBCFB* element increases the stability of the nonlinear solution procedure through its physical characteristics. The numerical robustness exhibited by the proposed

modeling methodology is attributed to the following reasons: The nonlinear procedure for the calculation of the internal forces of the *NBCFB* element, the stability induced by the consideration of shear and bending stiffness of the *NBCFB* elements, the modification of the concrete material model and the handling of the stress redistribution due to cracking.

The proposed modeling method managed to predict with adequate precision a number of experimental test results reported in the literature, illustrating its ability to predict failure loads, failure mechanisms and crack patterns with a high computational efficiency, regardless of the level of the load step of the incremental iterative nonlinear procedure. This is an important component when dealing with large-scale structures where the sensitivity on the required number of load increments applied during the analysis plays a crucial role in the feasibility of detailed finite element simulation of real-scale RC structures.

Acknowledgements

The financial support of the John Argyris Foundation (JAF) and the Research Funding Department (ELE) of NTUA provided to the first author is gratefully acknowledged. The author would like to acknowledge G. Stavroulakis for his contribution by providing the software code which was used during the pre-processing of the FE models and M. Fragiadakis and K. Papanikolopoulos for their helpful suggestions during the preparation of this work. Furthermore, they would like to acknowledge I. Lefas and V. Georgianou for providing the pictures of the crack patterns of the shear wall.

References

- Argyris, J., Tenek, L. and Olofsson, L. (1997), "TRIC: a simple but sophisticated 3-node triangular element based on 6 rigid-body and 12 straining modes for fast computational simulations of arbitrary isotropic and laminated composite shells", *Comput. Methods Appl. Mech. Eng.*, **145**, 11-85.
- Argyris, J.H., Balmer, H., Doltsinis, J.S., Dunne, P.C., Haase, M., Kleiber, M., Malejannakis, G.A., Mlejnek, H.P., Muller, M. and Scharf, D.W. (1979), "Finite element method - the natural approach", *Comput. Methods Appl. Mech. Eng.*, **17**(18), 1-106.
- Argyris, J.H., Tenek, L. and Mattsson, A. (1998), "BEC: A 2-node fast converging shear-deformable isotropic and composite beam element based on 6 rigid-body and 6 straining modes", *Comput. Methods Appl. Mech. Eng.*, **152**, 281-336.
- Armero, F. and Oller, S. (2000), "A general framework for continuum damage models. I. Infinitesimal plastic damage models in stress space", *Int. J. Solids Struct.*, **37**(48-50), 7409-7436.
- Balan, T.A., Spacone, E. and Kwon, M. (2001), "A 3D hypoplastic model for cyclic analysis of concrete structures", *Eng. Struct.*, **23**(4), 333-342.
- Barzegar, F. and Maddipudi, S. (1994), "Generating reinforcement in FE modeling of concrete structures", *J. Struct. Eng.*, **120**, 1656-1662.
- Bathe, K.J. (1995), *Finite Element Procedures*, Prentice Hall Inc., Upper Saddle River, New Jersey, USA.
- Bazant, Z.P. and Oh, B.H. (1983), "Crack band theory for fracture of concrete", *Mater. Construct.*, **16**(3), 155-177.
- Bazant, Z.P. and Zdenek, P. (1983), "Comment on orthotropic models for concrete and Geomaterials", *J. Eng. Mech.*, **109**(3), 849-865.
- Bertero, V.V., Aktan, A., Charney, F. and Sause, R. (1985), "Earthquake simulator tests and associated experimental analytical and correlation studies of one-fifth scale model", *Earthq. Effects on Reinforced*

- Concrete Structures, ACI, SP, Detroit, 375-424.
- Borja, R.I., Sama, K.M. and Sanz, P.F. (2003), "On the numerical integration of three-invariant elastoplastic constitutive models", *Comput. Methods Appl. Mech. Eng.*, **192**, 1227-1258.
- Bresel, B. and Scordelis, A.C. (1963), Shear strength of reinforced concrete beams, *ACI J.*, **60**, 51-74.
- Cedolin, L. and Dei, P.S. (1977), "Finite element studies of shear-critical R/C beams", *ASCE, J. Eng. Mech. Div.*, **103**(3), 395-410.
- Červenka, J. and Papanikolaou, V.K. (2008), "Three dimensional combined fracture-plastic material model for concrete", *Int. J. Plasticity*, **24**(12), 2192-2220.
- Červenka, V. (1970), Inelastic finite element analysis of reinforced concrete panels under plane loads, Ph.D., University of Colorado, University Microfilms, Inc., Michigan.
- Červenka, V., Jendele, L., Červenka, J. (2008), ATENA program documentation. Part 1: Theory, Červenka Consulting, Prague, Czech Republic.
- Cervera, M., Hinton, E. and Hassan, O. (1987), "Nonlinear Analysis of RC plate and shell structures using 20-noded isoparametric brick elements", *Comput. Struct.*, **25**, 845-869.
- Ciampi, V. and Nicoletti, M. (1986), "Parameter identification for cyclic constitutive models with stiffness and strength degradation", *Proceeding of the 8th European Conference on Earthquake Engineering*, Lisbon.
- Clough, R.W., Benuska, K.L. and Wilson, E.L. (1965), "Inelastic earthquake response of tall buildings", *Proceeding of the 3th World Conference on Earthquake Engineering*, New Zealand, 11, New Zealand.
- Cotsovos, D.M., Zeris, C.A. and Abas, A.A. (2009), "Finite Element Modeling of Structural Concrete", *ECCOMAS Thematic Conference on Computational Methods in Structural Dynamics and Earthquake Engineering*, COMPDYN 2009, Rhodes, Greece.
- Darwin, D. and Pecknold, D.A. (1976), "Analysis of RC shear panels under cyclic loading", *J. Struct. Div., ASCE*, **102**(2), 355-369.
- Desmorat, R., Gating, F. and Ragueneau, F. (2007), "Nonlocal anisotropic damage model and related computational aspects for quasi-brittle materials", *Eng. Fracture Mech.*, **74**(10), 1539-1560.
- Elwi, A.E. and Hrudey, T.M. (1989), "Finite element model for curved embedded reinforcement", *J. Eng. Mech.*, **115**, 740-754.
- Fardis, M.N., Alibe, B. and Tasoulas, J.L. (1983), "Monotonic and cyclic constitutive law for concrete", *J. Eng. Mech., ASCE*, **109**, 516-536.
- Girard, C. and Bastien, J. (2002), "Finite element bond slip model for concrete columns under cyclic loads", *J. Struct. Eng., ASCE*, **128**, 1502-1510.
- Gonzalez-Vidosa, F., Kotsovos, M.D. and Pavlovic, M.N. (1988), "On the numerical instability of the smeared-crack approach in the nonlinear modeling of concrete structures", *Commun. Appl. Num. Meth. Engng*, **4**, 799-806.
- Gonzalez-Vidosa, F., Kotsovos, M.D. and Pavlovic, M.N. (1991), "A three-dimensional nonlinear finite-element model for structural concrete; Part 1: main features and objectivity study and Part 2: generality study", *Proceedings of the Institution of Civil Engineers, Part 2, Research and Theory*, **91**, 517-544.
- Hartl, H. and Handel, C.H. (2002), "3D finite element modeling of reinforced concrete structures", fib 2002, Osaka Congress, Japan.
- Ile, N. and Reynouard, J.M. (2000), "Nonlinear analysis of reinforced concrete shear wall under earthquake loading", *J. Earthq. Eng.*, **4**(2), 183-213.
- Jason, L., Huerta, A., Pijaudier-Cabot, G. and Ghavamian, S. (2006), "An elastic plastic damage formulation for concrete: Application to elementary tests and comparison with an isotropic damage model", *Comput. Methods Appl. Mech. Eng.*, **195**(52), 7077-7092.
- Jendele, L. and Červenka, J. (2009), "On the solution of multi-point constraints – Application to FE analysis of reinforced concrete structures", *Comput. Struct.*, **87**, 970-980.
- Jiràsek, M. and Rolshoven, S. (2003), "Comparison of integral-type nonlocal plasticity models for strain-softening materials", *Int. J. Eng. Sci.*, **41**, 1553-1602.
- Kollegger, J. and Mehlhorn, G. (1987), "Material model for cracked reinforced concrete", IABSE Colloquium on Computational Mechanics of Concrete Structures—Advances and Applications, Delft, 63-74.

- Kotsovos, M.D. (1979), "A mathematical description of the strength properties of concrete under generalized stress", *Mag. Concrete Res.*, **31**(108), 151-158.
- Kotsovos, M.D. (1983), "Effect of Testing Techniques on the Post-Ultimate Behavior of Concrete in Compression", *Mater. Struct., RILEM*, **16**(91), 3-12.
- Kotsovos, M.D. (1984), "Concrete. A brittle fracturing material", *RILEM Mater. Struct.*, **17**, 107-115.
- Kotsovos, M.D. and Pavlovic, M.N. (1995), *Structural concrete. Finite Element Analysis for Limit State Design*, Thomas Telford, London.
- Kwak, H.G. and Kim, D.Y. (2001), "Nonlinear analysis of RC shear walls considering tension-stiffening effect", *Comput. Struct.*, **79**, 499-517.
- Kwak, H.G. and Kim, D.Y. (2001), "Nonlinear analysis of RC shear walls considering tension-stiffening effect", *Comput. Struct.*, **79**, 499-517.
- Kwak, H.G. and Kim, D.Y. (2004), "Material nonlinear analysis of RC shear walls subject to cyclic loadings", *Eng. Struct.*, **26**, 1423-1436.
- Kwak, H.G. and Kim, D.Y. (2006), "Cracking behavior of RC panels subject to biaxial tensile stresses", *Comput. Struct.*, **84**, 305-317.
- Kwan, W.P. and Billington, S.L. (2001), "Simulation of structural concrete under cyclic load", *J. Struct. Eng.*, **127**, 1391-1401.
- Lee, J. and Fenves, G.L. (2001), "A return-mapping algorithm for plastic-damage models: 3D and plane stress formulation", *Int. J. Numer. Methods Eng.*, **50**(2), 487-506.
- Lefas, I. (1988), Behavior of reinforced concrete walls and its implication for ultimate limit state design, Ph.D., University of London.
- Lefas, I.D. and Kotsovos, M.D. (1990), "Strength and deformation characteristics of reinforced concrete walls under load reversals", *ACI Struct. J.*, **87**(6), 716-726.
- Lublinter, J., Oliver, J., Oller, S. and Onate, E. (1989), "A plastic-damage model for concrete", *Int. J. Solids Struct.*, **3**, 299-326.
- Lykidis, G. (2007), Static and dynamic analysis of reinforced concrete structures with 3D finite elements and the smeared crack approach, Ph.D. Thesis, NTUA, Greece.
- Markou, G. (2010), ReConAn v1.00. Finite Element Analysis Software Manual, Institute of Structural Analysis and Seismic Research, Technical University of Athens, Greece.
- Markou, G. (2011), Detailed Three-Dimensional Nonlinear Hybrid Simulation for the Analysis of Large-Scale Reinforced Concrete Structures, Ph.D. Thesis, National Technical University of Athens.
- Markou, G. and Papadrakakis, M. (2012), "An efficient generation method of embedded reinforcement in hexahedral elements for reinforced concrete simulations", *Adv. Eng. Soft. ADES*, **45**(1), 175-187.
- Mazars, J., Kotronis, P., Ragueneau, F. and Casaux, G. (2006), "Using multifiber beams to account for shear and torsion. Applications to concrete structural elements", *Comput. Method Appl. Mech.*, **195**, 7264-7281.
- Mazars, J., Ragueneau, F., Casaux, G., Colombo, A. and Kotronis, P. (2004), "Numerical modeling for earthquake engineering: the case of lightly RC structural walls", *Int. J. Numer. Anal. Methods Geom.*, **28**, 857-874.
- Menegotto, M. and Pinto, P.E. (1973), "Method of analysis for cyclically loaded reinforced concrete plane frames Including changes in geometry and non-elastic behavior of elements under combined normal force and bending", Proceedings, IABSE Symposium on Resistance and Ultimate Deformability of Structures Acted on by Well Defined Repeated Loads, Lisbon.
- Mergos, P.E. and Kappos, A.J. (2008), "A distributed shear and flexural flexibility model with shear-flexure interaction for R/C members subjected to seismic loading", *Earthq. Eng. Struct. Dyn.*, **37**, 1349-1370.
- Mirzabozorg, H. and Ghaemian, M. (2005), "Nonlinear behavior of mass concrete in 3d problems using a smeared crack approach", *Earthq. Eng. Struct. Dyn.*, **34**, 247-269.
- Mitchell, W.F. (1997), "A Fortran 90 Interface for OpenGL", NISTIR 5985.
- Navarro, G.J., Miguel, S.P., Fernandez, P.M.A. and Filippou, F.C. (2007), "A 3D numerical model for reinforced and prestressed concrete elements subjected to combined axial, bending, shear and torsion loading", *Eng. Struct.*, **29**, 3404-3419.
- Nechnech, W., Meftah, F. and Reynouard, J.M. (2002), "An elasto-plastic damage model for plain concrete

- subjected to high temperatures”, *Eng. Struct.*, **24**(5) 597-611.
- Oliver, J., Linero, D.L., Huespe, A.E. and Manzoli, O.L. (2008), “Two-dimensional modeling of material failure in reinforced concrete by means of a continuum strong discontinuity approach”, *Comput. Methods Appl. Mech. Eng.*, **197**, 332-348.
- Oliver, J. (1989), “Consistent characteristic length for smeared cracking models”, *Int. J. Numer. Methods Eng.*, **28**(2), 461-474.
- Ozbolt, J. and Li, Y.J. (2001), “Three dimensional cyclic analysis of compressive diagonal shear failure”, *Finite Element Anal. RC Struct.*, Eds. (Willam, K., Tanabe, T.), ACI, SP, **205**(4), 61-79.
- Papachristidis, A., Fragiadakis, M., and Papadrakakis, M. (2009), “A shear-deformable fiber beam-column element for seismic analysis of steel structures”, *Computational Methods in Structural Dynamics and Earthquake Engineering (COMPDYN)*, Rhodes.
- Papachristidis, A., Fragiadakis, M., and Papadrakakis, M. (2010), “A 3D fibre beam-column element with shear modeling for the inelastic analysis of steel structures”, *Comput. Mech.*, **45**(6), 553-572.
- Papaoiannou, I., Fragiadakis, M. and Papadrakakis, M. (2005), “Inelastic analysis of framed structures using the fiber approach”, *Proceeding of the 5th International Congress on Computational Mechanics*, GRACM 05, Limassol, Cyprus, **1**, 231-238.
- Papanikolaou, V.K. and Kappos, A.J. (2009), “Numerical study of confinement effectiveness in solid and hollow reinforced concrete bridge piers: Part 1: Methodology”, *Eng. Struct.*, **87**(21-22), 1427-1439.
- Papanikolaou, V.K. and Kappos, A.J. (2009), “Numerical study of confinement effectiveness in solid and hollow reinforced concrete bridge piers: Part 2: Analysis results and discussion”, *Eng. Struct.*, **87**(21-22), 1427-1439.
- Papanikolopoulos, K. (2003), Investigation of the non-linear behavior of reinforced concrete members with finite elements, Postgraduate Thesis, National Technical University of Athens, Athens.
- Park, H. and Kim, J.Y. (2005), “Hybrid plasticity model for reinforced concrete in shear”, *Eng. Struct.*, **27**, 35-48.
- Rashid, Y.M. (1968), “Ultimate strength analysis of prestressed concrete vessels”, *Nucl. Eng. Des.*, **7**, 334-344.
- Saritas, A. and Filippou, F.C. (2009), “Numerical integration of a class of 3d plastic-damage concrete models and condensation of 3d stress-strain relations for use in beam finite elements”, *Eng. Struct.*, **31**(10), 2327-2336.
- Sato, Y. and Naganuma, K. (2007), “Discrete-like crack simulation by smeared crack-based FEM for reinforced concrete”, *Earthq. Eng. Struct. Dyn.*, **36**, 2137-2152.
- Siemens PLM Software (2009), World-class finite element analysis (FEA) solution for the Windows desktop, Siemens Product Lifecycle Management Software Inc.
- Simo, J.C. and Ju, J.W. (1987), “Strain-based and stress-based continuum damage models. I. formulation”, *Int. J. Solids Struct.*, **23**(7), 821-840.
- Spacone, E., Filippou, F.C. and Taucer, F.F. (1996), “Fibre beam-column model for nonlinear analysis of R/C frames Part I: formulation”, *Earthq. Eng. Struct. Dyn.*, **25**, 711-725.
- Spiliopoulos, K.V. and Lykidis, G. (2006), “An efficient three-dimensional solid finite element dynamic analysis of reinforced concrete structures”, *Earthq. Eng. Struct. Dyn.*, **35**, 137-157.
- Takizawa, H. (1976), “Notes on some basic problems in inelastic analysis of planar RC structures”, *Trans. Arch. Inst. Japan*, **240**, Part I, 51-62, Part II, 65-77.
- Taucer, F.F., Spacone, E. and Filippou, F.C. (1991), A Fiber beam-column element for seismic response analysis of reinforced concrete structures, Report No. UCB/EERC-91/17, University of California, Berkeley.
- Van Mier, J.G.M. (1986), “Multiaxial strain-softening of concrete”, *Mater. Struct., RILEM*, **19**(111), 179-200.
- Van Mier, J.G.M., Shah, S.P., Arnaud, M., Balayssac, J.P., Bassoul, A., Choi, S., Dasenbrock, D., Ferrara, G., French, C., Gobbi, M.E., Karihaloo, B.L., Konig, G., Kotsovov, M.D., Labnz, J., Lange-Kornbak, D., Markeset, G., Pavlovic, M.N., Simsch, G., Thienel, K.C., Turatsinze, A., Ulmer M., van Vliet, M.R.A. and Zissopoulos, D. (1997), “Test methods for the strain-softening of concrete”, Strain-softening of concrete in

- uniaxial compression”, *Mater. Struct., RILEM*, **30**(198), 195-209.
- Viwathatepa, S., Popov, E.P. and Bertero, V.V. (1979), *Effects of Generalized Loadings on Bond of Reinforcing Bars Embedded in Confined Concreteblocks*, Report to National Science Foundation, University of California Berkeley, California.
- Zeris, C.A. and Mahin, S. (1988), “Analysis of reinforced concrete beam-columns under uniaxial excitation”, *J. Struct. Eng., ASCE*, **114**(4), 804-820.

CC

Appendix A.

The algebraic algorithm for the computation of a line-plane intersection will be presented. A plane can be represented by the equation

$$Ax + By + Cz + D = 0 \tag{A1}$$

where (x, y, z) represent the coordinates of any point that lies on the plane.

Assuming that point $P1$ and $P2$ with coordinates $(x1, y1, z1)$ and $(x2, y2, z2)$, are two points defining the line, then the equation of the line can be written as

$$P = P1 + \lambda(P2 - P1) \tag{A2}$$

By substituting Eq. (A2) into Eq. (A1) results

$$A(x1 + \lambda(x2 - x1)) + B(y1 + \lambda(y2 - y1)) + C(z1 + \lambda(z2 - z1)) + D = 0 \tag{A3}$$

and by solving for λ

$$\lambda = \frac{A \cdot x1 + B \cdot y1 + C \cdot z1 + D}{A(x1 - x2) + B(y1 - y2) + C(z1 - z2)} \tag{A4}$$

There are two cases that we have to take under consideration regarding the value of λ . The first case is when this value is equal to zero which means that the normal of the plane is perpendicular to the line, therefore there is no intersection between them (Fig. A(b)). If λ is not equal to zero then there is an intersection between the line and the plane which is computed by substituting the expression of λ into Eq. (A2) (Fig. A(a)).

In addition to that, we have to check if the line is located on the plane. This can be easily performed by substituting the coordinates of the two points of the line into the equation of the plane (Eq. A(1)). If both coordinates satisfy the equation of the plane it means that the line is located on the plane (Fig. A(c)).

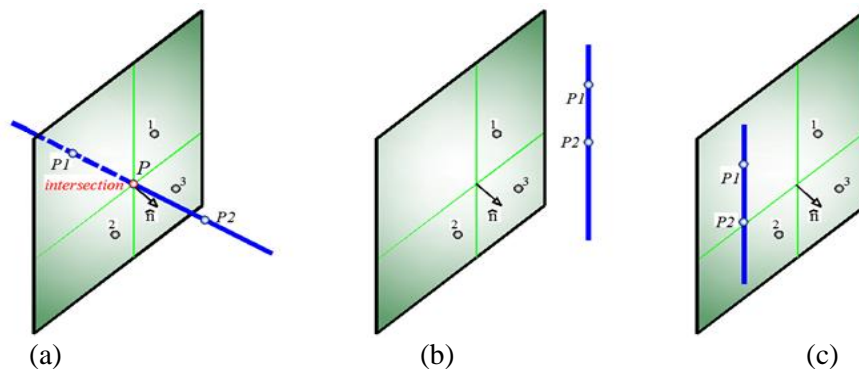


Fig. A Line-plane (a) intersection, (b) no intersection and (c) line is located on the plane

Appendix B.

The Barzegar and Maddipudi 1994 procedure for computing the natural coordinates of a virtual embedded rebar element node inside hexahedral concrete elements is described in this Appendix.

A point P_l with global coordinates $(x, y, z)_{P_l}$ on the initial rebar mesh (Fig. B), is contained in a given concrete element if its natural coordinates $\xi_{P_l}, \eta_{P_l}, \zeta_{P_l}$ satisfy the constraint

$$\xi_{P_l}, \eta_{P_l}, \zeta_{P_l} \leq 1 \quad (\text{B1})$$

associated with this particular hexahedral element.

In the isoparametric formulation the global coordinates (x, y, z) of a generic point within a solid element are expressed as

$$\begin{Bmatrix} x \\ y \\ z \end{Bmatrix} = \begin{bmatrix} N & \mathbf{0} & \mathbf{0} \\ \mathbf{0} & N & \mathbf{0} \\ \mathbf{0} & \mathbf{0} & N \end{bmatrix} \begin{Bmatrix} \mathbf{x}_i \\ \mathbf{y}_i \\ \mathbf{z}_i \end{Bmatrix} \quad (\text{B2})$$

where $\mathbf{x}_i, \mathbf{y}_i, \mathbf{z}_i$ are the global coordinate vectors of the hexahedral nodes and N represents the row vector of the displacement-shape functions.

Given that the natural coordinates $(\xi, \eta, \zeta)_{P_l}$ are the roots of

$$\begin{Bmatrix} x \\ y \\ z \end{Bmatrix}_{P_l} - \begin{bmatrix} N & \mathbf{0} & \mathbf{0} \\ \mathbf{0} & N & \mathbf{0} \\ \mathbf{0} & \mathbf{0} & N \end{bmatrix} \begin{Bmatrix} \xi \\ \eta \\ \zeta \end{Bmatrix}_{P_l} = \mathbf{0} \quad (\text{B3})$$

a NR iterative procedure is required in order to compute the solution of the above equation as follows

$$\begin{Bmatrix} \xi \\ \eta \\ \zeta \end{Bmatrix}_{P_l}^{n+1} = \begin{Bmatrix} \xi \\ \eta \\ \zeta \end{Bmatrix}_{P_l}^n + \begin{Bmatrix} \Delta \xi \\ \Delta \eta \\ \Delta \zeta \end{Bmatrix}_{P_l}^{n+1} \quad (\text{B4})$$

Since

$$\begin{Bmatrix} d\xi \\ d\eta \\ d\zeta \end{Bmatrix} = (\mathbf{J}^T)^{-1} \begin{Bmatrix} dx \\ dy \\ dz \end{Bmatrix} \quad (\text{B5})$$

where \mathbf{J} is the Jacobian matrix, the incremental natural coordinates are computed from

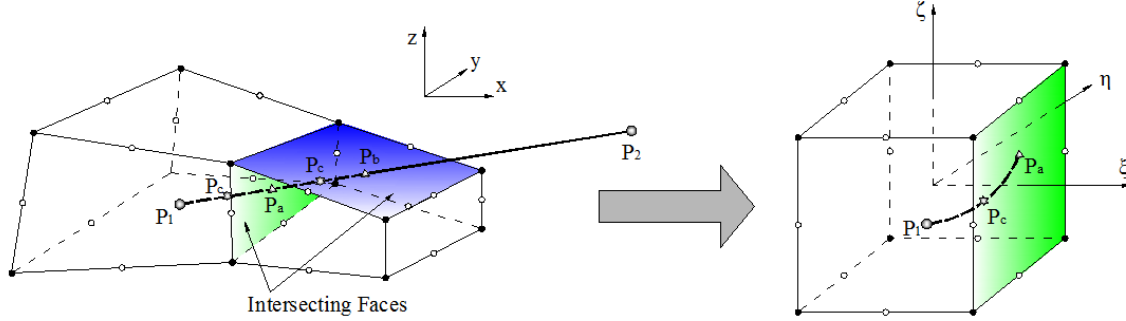


Fig. B Embedded reinforcement in hexahedral concrete element

$$\begin{Bmatrix} \Delta \xi \\ \Delta \eta \\ \Delta \zeta \end{Bmatrix}_{P_i}^{n+1} = (\mathbf{J}^{nT})^{-1} \begin{Bmatrix} x \\ y \\ z \end{Bmatrix}_{P_i} - \begin{bmatrix} \mathbf{N}^n & \mathbf{0} & \mathbf{0} \\ \mathbf{0} & \mathbf{N}^n & \mathbf{0} \\ \mathbf{0} & \mathbf{0} & \mathbf{N}^n \end{bmatrix} \begin{Bmatrix} x \\ y \\ z \end{Bmatrix} \quad (\text{B6})$$

with $\mathbf{J}^n = \mathbf{J}(\xi^n, \eta^n, \zeta^n)$; $\mathbf{N}^n = \mathbf{N}(\xi^n, \eta^n, \zeta^n)$.

Barzegar and Maddipudi 1994 found that the preceding solution scheme has a high convergence ratio which was also confirmed in this study. If the converged values do not satisfy (Eq. B1), the procedure proceeds to the next hexahedral element so as to check if the geometric constraint is satisfied (Eq. 7).

Appendix C.

The incremental-iterative nonlinear procedure for load increment k and NR iteration i can be described as follows:

1) Initialization.

Initialize all required variables including $k = 1, i = 1$.

2) Solve the global equation system and update the nodal displacement increments.

$$\Delta \mathbf{P}_E^k = (\mathbf{K}_{structure}^k)^{i-1} \cdot (\delta \Delta \boldsymbol{\rho}^k)^i \Rightarrow (\delta \Delta \boldsymbol{\rho}^k)^i = \left[(\mathbf{K}_{structure}^k)^{i-1} \right]^{-1} \cdot \Delta \mathbf{P}_E^k \quad (\text{C1})$$

If the NR iteration is greater than 1, then $\Delta \mathbf{P}_E^k$ corresponds to the unbalanced load vector $(\mathbf{P}_U^k)^{i-1}$ from the previous iteration. A check is performed if an update of the stiffness matrix is required before proceeding to the displacement calculation.

The calculated structural incremental displacements $(\delta \Delta \boldsymbol{\rho}^k)^i$ are added to the total displacement increments $(\Delta \boldsymbol{\rho}^k)^{i-1}$ of iteration $i-1$ to obtain the new displacement increment

$(\Delta \boldsymbol{\rho}^k)^i$ for iteration i inside the k -th load step

$$(\Delta \boldsymbol{\rho}^k)^i = (\Delta \boldsymbol{\rho}^k)^{i-1} + (\delta \Delta \boldsymbol{\rho}^k)^i \quad (\text{C2})$$

3) Compute the elements deformation increments.

By using the connection matrix \mathbf{a}_N and the direction cosine matrix \mathbf{T}_{04} the change in the element deformation increments which remain constant during loop j , is computed from the displacement increments.

$$\begin{matrix} (\delta \Delta \mathbf{q}^k)^i \\ (6 \times 1) \end{matrix} = \begin{matrix} \mathbf{a}_N \\ (6 \times 12) \end{matrix} \cdot \begin{matrix} \mathbf{T}_{04} \\ (12 \times 12) \end{matrix} \cdot \begin{matrix} (\delta \Delta \boldsymbol{\rho}^k)^i \\ (12 \times 1) \end{matrix} \quad (\text{C3})$$

4) Start the element state determination.

Set $j = 1$.

5) Compute the change in the element force increment.

For $j = 1$ the incremental force vector $\left((\delta \Delta \mathbf{Q}^k)^i \right)^1$ at load step k and iteration i is obtained from the element displacement increments $(\delta \Delta \mathbf{q}^k)^i$ for the current NR iteration i using the element natural stiffness matrix

$$\begin{matrix} \left((\delta \Delta \mathbf{Q}^k)^i \right)^1 \\ (6 \times 1) \end{matrix} = \begin{matrix} (\mathbf{K}_N^k)^{i-1} \\ (6 \times 6) \end{matrix} \cdot \begin{matrix} (\delta \Delta \mathbf{q}^k)^i \\ (6 \times 1) \end{matrix} \quad (\text{C4})$$

For $j > 1$ $\left((\delta \Delta \mathbf{Q}^k)^i \right)^j$ is obtained from the residual element deformation $\left((\mathbf{s}^k)^i \right)^{j-1}$ at the end of the previous element iteration $j-1$ and the corresponding element natural stiffness matrix.

$$\begin{matrix} \left((\delta \Delta \mathbf{Q}^k)^i \right)^j \\ (6 \times 1) \end{matrix} = \begin{matrix} \left((\mathbf{K}_N^k)^i \right)^{j-1} \\ (6 \times 6) \end{matrix} \cdot \begin{matrix} \left((\mathbf{s}^k)^i \right)^{j-1} \\ (6 \times 1) \end{matrix} \quad (\text{C5})$$

where

$$\begin{matrix} \left((\mathbf{s}^k)^i \right)^{j-1} \\ (6 \times 1) \end{matrix} = \int_0^L \mathbf{b}^T(\xi) \cdot \mathbf{r}^{j-1} d\xi \quad (\text{C6})$$

6) Update the element force increments and element resisting forces

The incremental force vector inside k -th load step, i -th iteration and j -th loop is updated as

$$\begin{matrix} \left((\Delta \mathbf{Q}^k)^i \right)^j \\ (6 \times 1) \end{matrix} = \begin{matrix} \left((\Delta \mathbf{Q}^k)^i \right)^{j-1} \\ (6 \times 1) \end{matrix} + \begin{matrix} \left((\delta \Delta \mathbf{Q}^k)^i \right)^j \\ (6 \times 1) \end{matrix} \quad (\text{C7})$$

and the current element resisting forces are calculated by adding the element force increments to the resisting force vector \mathbf{Q}^{k-1} of the previous load step $k-1$

$$\left(\underset{(6 \times 1)}{\mathbf{Q}^k} \right)^i = \underset{(6 \times 1)}{\mathbf{Q}^{k-1}} + \left(\underset{(6 \times 1)}{\Delta \mathbf{Q}^k} \right)^i \quad (\text{C8})$$

7) Compute the section force increments.

The elements section force increments are computed by using the interpolation functions $\mathbf{b}(\xi)$ defined at each Gauss-Lobato integration point as follows

$$\left(\underset{(3 \times 1)}{\delta \Delta \mathbf{D}^k(\xi)} \right)^i = \underset{(3 \times 6)}{\mathbf{b}(\xi)} \cdot \left(\underset{(6 \times 1)}{\delta \Delta \mathbf{Q}^k} \right)^i \quad (\text{C9})$$

$$\left(\underset{(3 \times 1)}{\Delta \mathbf{D}^k(\xi)} \right)^i = \left(\underset{(3 \times 1)}{\Delta \mathbf{D}^k(\xi)} \right)^{i-1} + \left(\underset{(3 \times 1)}{\delta \Delta \mathbf{D}^k(\xi)} \right)^i \quad (\text{C10})$$

and the total section forces by

$$\left(\underset{(3 \times 1)}{\mathbf{D}^k(\xi)} \right)^i = \underset{(3 \times 1)}{\mathbf{D}^{k-1}(\xi)} + \left(\underset{(3 \times 1)}{\Delta \mathbf{D}^k(\xi)} \right)^i \quad (\text{C11})$$

8) Compute the change in section deformation increments.

The change in the section deformation increments $\left(\delta \Delta \mathbf{d}^k(\xi) \right)^i$ is computed from

$$\left(\underset{(3 \times 1)}{\delta \Delta \mathbf{d}^k(\xi)} \right)^i = \left(\underset{(3 \times 1)}{\mathbf{r}^k(\xi)} \right)^{i-1} + \left(\underset{(3 \times 3)}{\mathbf{f}^k(\xi)} \right)^{i-1} \cdot \left(\underset{(3 \times 6)}{\mathbf{b}(\xi)} \right) \cdot \left(\underset{(6 \times 6)}{\mathbf{K}_N^k} \right)^{i-1} \cdot \left(\underset{(6 \times 1)}{\mathbf{s}^k} \right)^{i-1} \quad (\text{C12})$$

$$\left(\underset{(3 \times 1)}{\Delta \mathbf{d}^k(\xi)} \right)^i = \left(\underset{(3 \times 1)}{\Delta \mathbf{d}^k(\xi)} \right)^{i-1} + \left(\underset{(3 \times 1)}{\delta \Delta \mathbf{d}^k(\xi)} \right)^i \quad (\text{C13})$$

9) Compute the fiber deformation increments.

The fiber deformation increments are computed using the section compatibility matrix $\mathbf{I}(x)$ and the deformation increments as follows

$$\left(\underset{(1 \times 1)}{\delta \Delta \mathbf{e}^k(\xi)} \right)^i = \underset{(1 \times 3)}{\mathbf{I}(x)} \cdot \left(\underset{(3 \times 1)}{\delta \Delta \mathbf{d}^k(\xi)} \right)^i \quad (\text{C14})$$

then

$$\left(\left(\Delta \mathbf{e}^k(\xi) \right)^i \right)^j = \left(\left(\Delta \mathbf{e}^k(\xi) \right)^i \right)^{j-1} + \left(\left(\delta \Delta \mathbf{e}^k(\xi) \right)^i \right)^j \quad (\text{C15})$$

and the fiber deformations are updated by

$$\left(\left(\mathbf{e}^k(\xi) \right)^i \right)^j = \mathbf{e}^{k-1}(\xi) + \left(\left(\Delta \mathbf{e}^k(\xi) \right)^i \right)^j \quad (\text{C16})$$

10) Compute fiber stresses and update the tangent modulus of the fibers.

From the current fiber deformations of Eq. (C16), the fiber material model will provide the fiber normal stresses and the updated Young modulus of each fiber.

11) Compute the section tangent stiffness and flexibility matrices.

With the help of Eq. (17) the calculation of the current section tangent (or elastic) stiffness matrix $\left(\left(k^k(\xi) \right)^i \right)^j$ is performed following the estimation of the Young modulus for each fiber from step **10**. Then the section flexibility matrix is obtained from

$$\left(\left(\mathbf{e}^k(\xi) \right)^i \right)^j = \mathbf{e}^{k-1}(\xi) + \left(\left(\Delta \mathbf{e}^k(\xi) \right)^i \right)^j \quad (\text{C17})$$

12) Compute the section resisting forces.

The section internal resisting forces are derived explicitly from the fiber stresses according to Eq. (23).

13) Compute the sections unbalanced forces.

The difference between external applied loads and resisting forces results in the section unbalanced forces.

$$\left(\left(\mathbf{D}_U^k(\xi) \right)^i \right)^j = \left(\left(\mathbf{D}^k(\xi) \right)^i \right)^j - \left(\left(\mathbf{D}_R^k(\xi) \right)^i \right)^j \quad (\text{C18})$$

14) Compute the residual section deformations.

$$\left(\left(\mathbf{r}^k(\xi) \right)^i \right)^j = \left(\left(\mathbf{f}^k(\xi) \right)^i \right)^j \cdot \left(\left(\mathbf{D}_U^k(\xi) \right)^i \right)^j \quad (\text{C19})$$

15) Compute the element flexibility matrices.

The element flexibility matrix is computed by numerical integration on the beam section

following the Gauss-Lobato integration formula

$$\left(\left(\mathbf{F}^k \right)^i \right)^j_{(6 \times 6)} = \sum_{i_{sec}=1}^{tot.num.sec} \left[w_{i_{sec}} \cdot \mathbf{b}^T \left(\xi_{i_{sec}} \right)_{(6 \times 3)} \cdot \left(\left(\mathbf{f}^k \left(\xi_{i_{sec}} \right) \right)^i \right)^j_{(3 \times 3)} \cdot \mathbf{b} \left(\xi_{i_{sec}} \right)_{(3 \times 6)} \right] \quad (C20)$$

where *tot.num.sec* is the total number of Gauss-Lobato integration points (total number of control sections), $\xi_{i_{sec}}$ is the natural coordinate of the section along the beam length and $w_{i_{sec}}$ is the corresponding weight factor.

Finally, the element stiffness matrix is obtained by inverting the flexibility matrix $\left(\left(\mathbf{F}^k \right)^i \right)^j_{(5 \times 5)}$

$$\left(\left(\mathbf{K}^k \right)^i \right)^j_{(5 \times 5)} = \left[\left(\left(\mathbf{F}^k \right)^i \right)^j_{(5 \times 5)} \right]^{-1} \quad (C21)$$

while the main diagonal stiffness coefficient $\left(\left(\mathbf{K}(6,6)^k \right)^i \right)^j$ which corresponds to the torsional stiffness, is given by

$$\left(\left(\mathbf{K}(6,6)^k \right)^i \right)^j = \frac{GJ_p}{L} \quad (C22)$$

16) Check for element convergence.

The convergence criterion that was implemented in this work was an energy-based criterion given by

$$error = \frac{\left[\left(\left(\mathbf{s}^k \right)^i \right)^j \right]^T \cdot \left(\left(\mathbf{K}^k \right)^i \right)^j \cdot \left(\left(\mathbf{s}^k \right)^i \right)^j}{\left(\Delta \mathbf{q}^k \right)^T \cdot \left(\left(\mathbf{K}^k \right)^i \right)^1 \cdot \left(\Delta \mathbf{q}^k \right)} \quad (C23)$$

where \mathbf{s}^k is the residual element deformation and the tolerance was set to 10^{-16} (Taucer 1991).

$$\left(\left(\mathbf{s}^k \right)^i \right)^j_{(6 \times 1)} = \sum_{i_{sec}=1}^{tot.num.sec} \left[weight_{i_{sec}} \cdot \mathbf{b}^T \left(\xi_{i_{sec}} \right)_{(6 \times 3)} \cdot \left(\left(\mathbf{r}^k \left(\xi_{i_{sec}} \right) \right)^i \right)^j_{(3 \times 1)} \right] \quad (C24)$$

If the convergence criterion is satisfied then proceed to the next step, otherwise return to step 5 and increase *j* by 1.

17) Compute the resisting forces of each element and the internal forces of the structure.

When the equilibrium conditions are satisfied for all *NBCFB* elements, the *i*-th NR iteration is

completed regarding the calculation of the internal forces at structural level. The internal forces of the structure $(\mathbf{P}_R^k)^i$ are calculated by assembling all element internal forces $(\mathbf{Q}_{ele}^k)^i$ (Eq. C8) according to the expression

$$\begin{pmatrix} \mathbf{P}_{ele}^k \\ (12 \times 1) \end{pmatrix}^i = \begin{pmatrix} \mathbf{T}_{04}^T \\ (12 \times 12) \end{pmatrix} \cdot \begin{pmatrix} \mathbf{a}_n^T \\ (12 \times 6) \end{pmatrix} \cdot \begin{pmatrix} \mathbf{Q}_{ele}^k \\ (6 \times 1) \end{pmatrix}^i, \quad (\text{C25a})$$

then

$$\begin{pmatrix} \mathbf{P}_R^k \\ (12 \times 1) \end{pmatrix}^i = \sum_{iele=1}^{num.ele} \begin{pmatrix} \mathbf{P}_{iele}^k \\ (6 \times 1) \end{pmatrix}^i \quad (\text{C25b})$$

18) Update structure's stiffness matrix.

The structural stiffness matrix is updated by assembling the element stiffness matrices

$$\begin{pmatrix} \mathbf{K}_{ele}^k \\ (12 \times 12) \end{pmatrix}^i = \begin{pmatrix} \mathbf{T}_{04}^T \\ (12 \times 12) \end{pmatrix} \cdot \begin{pmatrix} \mathbf{a}_n^T \\ (12 \times 6) \end{pmatrix} \cdot \begin{pmatrix} \mathbf{K}_N^k \\ (6 \times 6) \end{pmatrix} \cdot \begin{pmatrix} \mathbf{a}_n \\ (6 \times 12) \end{pmatrix} \cdot \begin{pmatrix} \mathbf{T}_{04} \\ (12 \times 12) \end{pmatrix}, \quad (\text{C26a})$$

then

$$\begin{pmatrix} \mathbf{K}_S^k \\ (12 \times 12) \end{pmatrix}^i = \sum_{iele=1}^{num.ele} \begin{pmatrix} \mathbf{K}_{ele}^k \\ (12 \times 12) \end{pmatrix}^i \quad (\text{C27b})$$

19) Compute the unbalanced forces of the structure.

$$\begin{pmatrix} \mathbf{P}_U^k \\ (12 \times 1) \end{pmatrix}^i = \mathbf{P}^k - \begin{pmatrix} \mathbf{P}_R^k \\ (12 \times 1) \end{pmatrix}^i \quad (\text{C28})$$

where \mathbf{P}^k is the total applied load at load increment k

$$\mathbf{P}_E^k = \mathbf{P}^{k-1} + \Delta \mathbf{P}_E^k \quad (\text{C29})$$

20) Check for global convergence.

If the convergence criterion is satisfied at the structural level, then $k=k+1$ and proceed to the next load increment, otherwise set $i = i + 1$ and return to step 2 for the $i+1$ NR iteration. In this work, an energy based convergence criterion was used with tolerance 10^{-4} .

It is obvious that, the use of *NBCFB* elements for the simulation of the reinforcement is penalized with an increased computational effort compared to the much simpler rod element. The computational effort depends on the number of fibers and Gauss-Lobato integration points used for the calculation of the stiffness matrix. Following a numerical parametric investigation it was concluded that 2 to 3 Gauss-Lobato integration points along the axis of the element combined with 4 fibers per section (Fig. 15), are adequate for ensuring both numerical accuracy and

computational efficiency. It is important to note that, the combination of the natural mode formulation (Argyris *et al.* 1998) with the force-based approach provides an elegant framework for the calculation of the stiffness matrix with substantial savings in the required CPU time (Papaioannou *et al.* 2005, Papachristidis *et al.* 2009, 2010).

Appendix D.

In order to estimate the translational modes ρ as functions of the displacements and rotations at vertices 1, 2 and 3 of a triangle (Fig. 3), it is assumed that the linear displacement field with respect to the local elemental coordinates can be described as

$$u = p_o + p_1x + p_2y, \quad v = q_o + q_1x + q_2y, \quad w = r_o \quad (D1)$$

where p_i, q_i, r_i are the displacements referred to the local coordinate system. If the origin of the local coordinate system is placed at the element's barycenter, Eqs. 1 may be written in the form

$$u_1 + u_2 + u_3 = 3p_o, \quad v_1 + v_2 + v_3 = 3q_o, \quad w_1 + w_2 + w_3 = 3r_o \quad (D2)$$

The rigid body drilling rotation ρ_{06} is given by

$$\rho_{06} = \frac{1}{2} \left(\frac{\partial v}{\partial x} - \frac{\partial u}{\partial y} \right) = \frac{1}{2} (q_1 - p_2) \quad (D3)$$

If we write Eqs. D1 for every vertex, the quantity in Eq. (D3) becomes

$$\rho_{06} = -\frac{1}{2\Omega} (x_a u_1 + y_a v_1 + x_\beta u_2 + y_\beta v_2 + x_\gamma u_3 + y_\gamma v_3) \quad (D4)$$

where

$$x_\alpha = x_3 - x_2, \quad x_\beta = x_1 - x_3, \quad x_\gamma = x_2 - x_1, \quad y_\alpha = y_3 - y_2, \quad y_\beta = y_1 - y_3, \quad y_\gamma = y_2 - y_1 \quad (D5)$$

and x_i, y_i ($i = 1, 3$ master triangle nodes) are the local Cartesian nodal coordinates of the triangle (Fig. 3) while Ω is the area of the triangle. Then the relation between the rigid body rotations ρ_{04}, ρ_{05} and the Cartesian coordinates of the triangle vertices need to be defined. For this purpose the rotation θ_1 of the triangle along the side 23, as depicted in Fig. 3, is given by

$$\theta_1 = \frac{w_1}{h_a} = \frac{w_1 l_a}{2\Omega} \quad (D6)$$

and its two components, which project to the local Cartesian axes, are given by

$$\theta_{1x} = \theta_1 \cos a_x = \theta_1 \frac{x_a}{l_a} = \frac{x_a}{2\Omega} w_1, \quad \theta_{1y} = \theta_1 \sin a_y = \theta_1 \frac{y_a}{l_a} = \frac{y_a}{2\Omega} w_1 \quad (D7)$$

Similarly

$$\theta_{2x} = \frac{x_\beta}{2\Omega} w_2, \quad \theta_{3x} = \frac{x_\gamma}{2\Omega} w_3, \quad \theta_{2y} = \frac{y_\beta}{2\Omega} w_2, \quad \theta_{3y} = \frac{y_\gamma}{2\Omega} w_3 \quad (\text{D8})$$

Therefore, the rigid-body rotations ρ_{04}, ρ_{05} are simply

$$\rho_{04} = \theta_{1x} + \theta_{2x} + \theta_{3x}, \quad \rho_{05} = \theta_{1y} + \theta_{2y} + \theta_{3y} \quad (\text{D9})$$

$$\rho_{04} = \frac{x_a}{2\Omega} w_1 + \frac{x_\beta}{2\Omega} w_2 + \frac{x_\gamma}{2\Omega} w_3, \quad \rho_{05} = \frac{y_a}{2\Omega} w_1 + \frac{y_\beta}{2\Omega} w_2 + \frac{y_\gamma}{2\Omega} w_3 \quad (\text{D10})$$

The above equations can be expressed in matrix form

$$\begin{Bmatrix} \rho_{04} \\ \rho_{05} \\ \rho_{06} \end{Bmatrix} = \begin{bmatrix} \bar{\mathbf{R}}_1^j & \bar{\mathbf{R}}_2^j & \bar{\mathbf{R}}_3^j \\ (3 \times 3) & (3 \times 3) & (3 \times 3) \end{bmatrix} \begin{Bmatrix} \mathbf{x} \\ \mathbf{y} \\ \mathbf{z} \end{Bmatrix} \quad (\text{D11})$$

$$\bar{\mathbf{R}}_1^j = \begin{bmatrix} 0 & 0 & \frac{x_a}{2\Omega} \\ 0 & 0 & \frac{y_a}{2\Omega} \\ -\frac{x_a}{2\Omega} & -\frac{y_a}{2\Omega} & 0 \end{bmatrix}, \quad \bar{\mathbf{R}}_2^j = \begin{bmatrix} 0 & 0 & \frac{x_\beta}{2\Omega} \\ 0 & 0 & \frac{y_\beta}{2\Omega} \\ -\frac{x_\beta}{2\Omega} & -\frac{y_\beta}{2\Omega} & 0 \end{bmatrix}, \quad \bar{\mathbf{R}}_3^j = \begin{bmatrix} 0 & 0 & \frac{x_\gamma}{2\Omega} \\ 0 & 0 & \frac{y_\gamma}{2\Omega} \\ -\frac{x_\gamma}{2\Omega} & -\frac{y_\gamma}{2\Omega} & 0 \end{bmatrix} \quad (\text{D12})$$

and $j = 1, 2$ corresponds to the embedded rebar beam nodes and Ω is the area of the corresponding master triangle. $\mathbf{x}, \mathbf{y}, \mathbf{z}$ are the translational displacement vectors of the master triangle.

These local rotation matrices are transformed to the \mathbf{R}_m^j in the global coordinate system using the standard cosine transformation matrix in 3D.

$$\mathbf{R}_m^j = \mathbf{T}_o^T \bar{\mathbf{R}}_m^j \mathbf{T}_o \quad (\text{D13})$$

Then for each master triangle the computation of the transformation matrix \mathbf{T} (12x24) of Eq. (2), which is used to connect the hexahedral nodal displacements with the corresponding embedded beam nodal displacements (Eq. (1)), is completed.